Observation of exclusive dijet production at the Fermilab Tevatron (p)over-bar-p collider

T. Aaltonen, J. Adelman, T. Akimoto, M. G. Albrow, B. A. Gonzalez, S. Amerio, D. Amidei, A. Anastassov, A. Annovi, J. Antos, M. Aoki, G. Apollinari, A. Apresyan, T. Arisawa, A. Artikov, W. Ashmanskas, A. Attal, A. Aurisano, F. Azfar, P. Azzi-Bacchetta, P. Azzurri, N. Bacchetta, W. Badgett, A. Barbaro-Galtieri, V. E. Barnes, B. A. Barnett, S. Baroiant, V. Bartsch, G. Bauer, P. H. Beauchemin, F. Bedeschi, P. Bednar, S. Behari, G. Bellettini, J. Bellinger, A. Belloni, D. Benjamin, A. Beretvas, J. Beringer, T. Berry, A. Bhatti, M. Binkley, D. Bisello, I. Bizjak, R. E. Blair, C. Blocker, B. Blumenfeld, A. Bocci, A. Bodek, V. Boisvert, G. Bolla, A. Bolshov, D. Bortoletto, J. Boudreau, A. Boveia, B. Brau, A. Bridgeman, L. Brigliadori, C. Bromberg, E. Brubaker, J. Budagov, H. S. Budd, S. Budd, K. Burkett, G. Busetto, P. Bussey, A. Buzatu, K. L. Byrum, S. Cabrera, M. Campanelli, M. Campbell, F. Canelli, A. Canepa, D. Carlsmith, R. Carosi, S. Carrillo, S. Carron, B. Casal, M. Casarsa, A. Castro, P. Catastini, D. Cauz, M. Cavalli-Sforza, A. Cerri, L. Cerrito, S. H. Chang, Y. C. Chen, M. Chertok, G. Chiarelli, G. Chlachidze, F. Chlebana, K. Cho, D. Chokheli, J. P. Chou, G. Choudalakis, S. H. Chuang, K. Chung, W. H. Chung, Y. S. Chung, C. I. Ciobanu, M. A. Ciocci, A. Clark, D. Clark, G. Compostella, M. E. Convery, J. Conway, B. Cooper, K. Copic, M. Cordelli, G. Cortiana, F. Crescioli, C. C. Almenar, J. Cuevas, R. Culbertson, J. C. Cully, D. Dagenhart, M. Datta, T. Davies, P. de Barbaro, S. De Cecco, A. Deisher, G. De Lentdecker, G. De Lorenzo, M. Dell'Orso, L. Demortier, J. Deng, M. Deninno, D. De Pedis, P. F. Derwent, G. P. Di Giovanni, C. Dionisi, B. Di Ruzza, J. R. Dittmann, M. D'Onofrio, S. Donati, P. Dong, J. Donini, T. Dorigo, S. Dube, J. Efron, R. Erbacher, D. Errede, S. Errede, R. Eusebi, H. C. Fang, S. Farrington, W. T. Fedorko, R. G. Feild, M. Feindt, J. P. Fernandez, C. Ferrazza, R. Field, G. Flanagan, R. Forrest, S. Forrester, M. Franklin, J. C. Freeman, I. Furic, M. Gallinaro, J. Galyardt, F. Garberson, J. E. Garcia, A. F. Garfinkel, K. Genser, H. Gerberich, D. Gerdes, S. Giagu, V. Giakoumopolou, P. Giannetti, K. Gibson, J. L. Gimmell, C. M. Ginsburg, N. Giokaris, M. Giordani, P. Giromini,

M. Giunta, V. Glagolev, D. Glenzinski, M. Gold, N. Goldschmidt, A. Golossanov, G. Gomez, G. Gomez-Ceballos, M. Goncharov, O. G. Lez, I. Gorelov, A. T. Goshaw, K. Goulianos, A. Gresele, S. Grinstein, C. Grosso-Pilcher, R. C. Group, U. Grundler, J. G. da Costa, Z. Gunay-Unalan, C. Haber, K. Hahn, S. R. Hahn, E. Halkiadakis, A. Hamilton, B. Y. Han, J. Y. Han, R. Handler, F. Happacher, K. Hara, D. Hare, M. Hare, S. Harper, R. F. Harr, R. M. Harris, M. Hartz, K. Hatakeyama, J. Hauser, C. Hays, M. Heck, A. Heijboer, B. Heinemann, J. Heinrich, C. Henderson, M. Herndon, J. Heuser, S. Hewamanage, D. Hidas, C. S. Hill, D. Hirschbuehl, A. Hocker, S. Hou, M. Houlden, S. C. Hsu, B. T. Huffman, R. E. Hughes, U. Husemann, J. Huston, J. Incandela, G. Introzzi, M. Iori, A. Ivanov, B. Iyutin, E. James, B. Jayatilaka, D. Jeans, E. J. Jeon, S. Jindariani, W. Johnson, M. Jones, K. K. Joo, S. Y. Jun, J. E. Jung, T. R. Junk, T. Kamon, D. Kar, P. E. Karchin, Y. Kato, R. Kephart, U. Kerzel, V. Khotilovich, B. Kilminster, D. H. Kim, H. S. Kim, J. E. Kim, M. J. Kim, S. B. Kim, S. H. Kim, Y. K. Kim, N. Kimura, L. Kirsch, S. Klimenko, M. Klute, B. Knuteson, B. R. Ko, S. A. Koay, K. Kondo, D. J. Kong, J. Konigsberg, A. Korytov, A. V. Kotwal, J. Kraus, M. Kreps, J. Kroll, N. Krumnack, M. Kruse, V. Krutelyov, T. Kubo, S. E. Kuhlmann, T. Kuhr, N. P. Kulkarni, Y. Kusakabe, S. Kwang, A. T. Laasanen, S. Lai, S. Lami, S. Lammel, M. Lancaster, R. L. Lander, K. Lannon, A. Lath, G. Latino, I. Lazzizzera, T. LeCompte, J. Lee, J. Lee, Y. J. Lee, S. W. Lee, R. Lefevre, N. Leonardo, S. Leone, S. Levy, J. D. Lewis, C. Lin, C. S. Lin, J. Linacre, M. Lindgren, E. Lipeles, A. Lister, D. O. Litvintsev, T. Liu, N. S. Lockyer, A. Loginov, M. Loreti, L. Lovas, R. S. Lu, D. Lucchesi, J. Lueck, C. Luci, P. Lujan, P. Lukens, G. Lungu, L. Lyons, J. Lys, R. Lysak, E. Lytken, P. Mack, D. MacQueen, R. Madrak, K. Maeshima, K. Makhoul, T. Maki, P. Maksimovic, S. Malde, S. Malik, G. Manca, A. Manousakis, F. Margaroli, C. Marino, C. P. Marino, A. Martin, M. Martin, V. Martin, M. Martiinez, R. Martiinez-Ballariin, T. Maruyama, P. Mastrandrea, T. Masubuchi, M. E. Mattson, P. Mazzanti, K. S. McFarland, P. McIntyre, R. McNulty, A. Mehta, P. Mehtala, S. Menzemer, A. Menzione, P. Merkel, C. Mesropian, A. Messina, T. Miao, N. Miladinovic, J. Miles, R. Miller, C. Mills, M. Milnik, A. Mitra, G. Mitselmakher, H. Miyake, S. Moed, N. Moggi, C. S. Moon, R. Moore, M. Morello, P. M. Fernandez, J. Muulmenstaadt, A. Mukherjee, T. Muller, R. Mumford, P. Murat, M. Mussini, J. Nachtman, Y. Nagai, A. Nagano, J. Naganoma, K. Nakamura, I. Nakano, A. Napier, V. Necula, C. Neu, M. S. Neubauer, J. Nielsen, L. Nodulman, M. Norman, O. Norniella, E. Nurse, S. H. Oh, Y. D. Oh, I. Oksuzian, T. Okusawa, R. Oldeman, R. Orava, K. Osterberg, S. P. Griso, C. Pagliarone, E. Palencia, V. Papadimitriou, A. Papaikonomou, A. A. Paramonov, B. Parks, S. Pashapour, J. Patrick, G. Pauletta, M. Paulini, C. Paus, D. E. Pellett, A. Penzo, T. J. Phillips, G. Piacentino, J. Piedra, L. Pinera, K. Pitts, C. Plager, L. Pondrom, X. Portell, O. Poukhov, N. Pounder, F. Prakoshyn, A. Pronko, J. Proudfoot, F. Ptohos, G. Punzi, J. Pursley, J. Rademacker, A. Rahaman, V. Ramakrishnan, N. Ranjan, I. Redondo, B. Reisert, V. Rekovic, P. Renton, M. Rescigno, S. Richter, F. Rimondi, L. Ristori, A. Robson, T. Rodrigo, E. Rogers, S. Rolli, R. Roser, M. Rossi, R. Rossin, P. Roy, A. Ruiz, J. Russ, V. Rusu, H. Saarikko, A. Safonov, W. K. Sakumoto, G. Salamanna, O. Salto, L. Santi, S.

Sarkar, L. Sartori, K. Sato, A. Savoy-Navarro, T. Scheidle, P. Schlabach, E. E. Schmidt, M. A. Schmidt, M. P. Schmidt, M. Schmitt, T. Schwarz, L. Scodellaro, A. L. Scott, A. Scribano, F. Scuri, A. Sedov, S. Seidel, Y. Seiya, A. Semenov, L. Sexton-Kennedy, A. Sfyria, S. Z. Shalhout, M. D. Shapiro, T. Shears, P. F. Shepard, D. Sherman, M. Shimojima, M. Shochet, Y. Shon, I. Shreyber, A. Sidoti, P. Sinervo, A. Sisakyan, A. J. Slaughter, J. Slaunwhite, K. Sliwa, J. R. Smith, F. D. Snider, R. Snihur, M. Soderberg, A. Soha, S. Somalwar, V. Sorin, J. Spalding, F. Spinella, T. Spreitzer, P. Squillacioti, M. Stanitzki, R. S. Denis, B. Stelzer, O. Stelzer-Chilton, D. Stentz, J. Strologas, D. Stuart, J. S. Suh, A. Sukhanov, H. Sun, I. Suslov, T. Suzuki, A. Taffard, R. Takashima, Y. Takeuchi, R. Tanaka, M. Tecchio, P. K. Teng, K. Terashi, J. Thom, A. S. Thompson, G. A. Thompson, E. Thomson, P. Tipton, V. Tiwari, S. Tkaczyk, D. Toback, S. Tokar, K. Tollefson, T. Tomura, D. Tonelli, S. Torre, D. Torretta, S. Tourneur, W. Trischuk, Y. Tu, N. Turini, F. Ukegawa, S. Uozumi, S. Vallecorsa, N. Van Remortel, A. Varganov, E. Vataga, F. Vazquez, G. Velev, C. Vellidis, V. Veszpremi, M. Vidal, R. Vidal, I. Vila, R. Vilar, T. Vine, M. Vogel, I. Volobouev, G. Volpi, F. Wurthwein, P. Wagner, R. G. Wagner, R. L. Wagner, J. Wagner-Kuhr, W. Wagner, T. Wakisaka, R. Wallny, S. M. Wang, A. Warburton, D. Waters, M. Weinberger, W. C. Wester, B. Whitehouse, D. Whiteson, A. B. Wicklund, E. Wicklund, G. Williams, H. H. Williams, P. Wilson, B. L. Winer, P. Wittich, S. Wolbers, C. Wolfe, T. Wright, X. Wu, S. M. Wynne, A. Yagil, K. Yamamoto, J. Yamaoka, T. Yamashita, C. Yang, U. K. Yang, Y. C. Yang, W. M. Yao, G. P. Yeh, J. Yoh, K. Yorita, T. Yoshida, G. B. Yu, I. Yu, S. S. Yu, J. C. Yun, L. Zanello, A. Zanetti, I. Zaw, X. Zhang, Y. Zheng, and S. Zucchelli

Observation of exclusive dijet production at the Fermilab Tevatron $\bar{p}p$ collider

T. Aaltonen,[23] J. Adelman,[13] T. Akimoto,[54] M. G. Albrow,[17] B. Álvarez González,[11] S. Amerio,[42] D. Amidei,[34]
A. Anastassov,[51] A. Annovi,[19] J. Antos,[14] M. Aoki,[24] G. Apollinari,[17] A. Apresyan,[47] T. Arisawa,[56] A. Artikov,[15]
W. Ashmanskas,[17] A. Attal,[3] A. Aurisano,[52] F. Azfar,[41] P. Azzi-Bacchetta,[42] P. Azzurri,[45] N. Bacchetta,[42] W. Badgett,[17]
A. Barbaro-Galtieri,[28] V. E. Barnes,[47] B. A. Barnett,[25] S. Baroiant,[7] V. Bartsch,[30] G. Bauer,[32] P.-H. Beauchemin,[33]
F. Bedeschi,[45] P. Bednar,[14] S. Behari,[25] G. Bellettini,[45] J. Bellinger,[58] A. Belloni,[22] D. Benjamin,[16] A. Beretvas,[17]
J. Beringer,[28] T. Berry,[29] A. Bhatti,[49] M. Binkley,[17] D. Bisello,[42] I. Bizjak,[30] R. E. Blair,[2] C. Blocker,[6] B. Blumenfeld,[25]
A. Bocci,[16] A. Bodek,[48] V. Boisvert,[48] G. Bolla,[47] A. Bolshov,[32] D. Bortoletto,[47] J. Boudreau,[46] A. Boveia,[10] B. Brau,[10]
A. Bridgeman,[24] L. Brigliadori,[5] C. Bromberg,[35] E. Brubaker,[13] J. Budagov,[15] H. S. Budd,[48] S. Budd,[24] K. Burkett,[17]
G. Busetto,[42] P. Bussey,[21] A. Buzatu,[33] K. L. Byrum,[2] S. Cabrera,[16,r] M. Campanelli,[35] M. Campbell,[34] F. Canelli,[17]
A. Canepa,[44] D. Carlsmith,[58] R. Carosi,[45] S. Carrillo,[18,l] S. Carron,[33] B. Casal,[11] M. Casarsa,[17] A. Castro,[5] P. Catastini,[45]
D. Cauz,[53] M. Cavalli-Sforza,[3] A. Cerri,[28] L. Cerrito,[30,q] S. H. Chang,[27] Y. C. Chen,[1] M. Chertok,[7] G. Chiarelli,[45]
G. Chlachidze,[17] F. Chlebana,[17] K. Cho,[27] D. Chokheli,[15] J. P. Chou,[22] G. Choudalakis,[32] S. H. Chuang,[51] K. Chung,[12]
W. H. Chung,[58] Y. S. Chung,[48] C. I. Ciobanu,[24] M. A. Ciocci,[45] A. Clark,[20] D. Clark,[6] G. Compostella,[42] M. E. Convery,[17]
J. Conway,[7] B. Cooper,[30] K. Copic,[34] M. Cordelli,[19] G. Cortiana,[42] F. Crescioli,[45] C. Cuenca Almenar,[7,r] J. Cuevas,[11,o]
R. Culbertson,[17] J. C. Cully,[34] D. Dagenhart,[17] M. Datta,[17] T. Davies,[21] P. de Barbaro,[48] S. De Cecco,[50] A. Deisher,[28]
G. De Lentdecker,[48,d] G. De Lorenzo,[3] M. Dell'Orso,[45] L. Demortier,[49] J. Deng,[16] M. Deninno,[5] D. De Pedis,[50]
P. F. Derwent,[17] G. P. Di Giovanni,[43] C. Dionisi,[50] B. Di Ruzza,[53] J. R. Dittmann,[4] M. D'Onofrio,[3] S. Donati,[45] P. Dong,[8]
J. Donini,[42] T. Dorigo,[42] S. Dube,[51] J. Efron,[38] R. Erbacher,[7] D. Errede,[24] S. Errede,[24] R. Eusebi,[17] H. C. Fang,[28]
S. Farrington,[29] W. T. Fedorko,[13] R. G. Feild,[59] M. Feindt,[26] J. P. Fernandez,[31] C. Ferrazza,[45] R. Field,[18] G. Flanagan,[47]
R. Forrest,[7] S. Forrester,[7] M. Franklin,[22] J. C. Freeman,[28] I. Furic,[18] M. Gallinaro,[49] J. Galyardt,[12] F. Garberson,[10]
J. E. Garcia,[45] A. F. Garfinkel,[47] K. Genser,[17] H. Gerberich,[24] D. Gerdes,[34] S. Giagu,[50] V. Giakoumopolou,[45,a]
P. Giannetti,[45] K. Gibson,[46] J. L. Gimmell,[48] C. M. Ginsburg,[17] N. Giokaris,[15,a] M. Giordani,[53] P. Giromini,[19] M. Giunta,[45]
V. Glagolev,[15] D. Glenzinski,[17] M. Gold,[36] N. Goldschmidt,[18] A. Golossanov,[17] G. Gomez,[11] G. Gomez-Ceballos,[32]
M. Goncharov,[52] O. González,[31] I. Gorelov,[36] A. T. Goshaw,[16] K. Goulianos,[49] A. Gresele,[42] S. Grinstein,[22]
C. Grosso-Pilcher,[13] R. C. Group,[17] U. Grundler,[24] J. Guimaraes da Costa,[22] Z. Gunay-Unalan,[35] C. Haber,[28] K. Hahn,[32]
S. R. Hahn,[17] E. Halkiadakis,[51] A. Hamilton,[20] B.-Y. Han,[48] J. Y. Han,[48] R. Handler,[58] F. Happacher,[19] K. Hara,[54]
D. Hare,[51] M. Hare,[55] S. Harper,[41] R. F. Harr,[57] R. M. Harris,[17] M. Hartz,[46] K. Hatakeyama,[49] J. Hauser,[8] C. Hays,[41]
M. Heck,[26] A. Heijboer,[44] B. Heinemann,[28] J. Heinrich,[44] C. Henderson,[32] M. Herndon,[58] J. Heuser,[26] S. Hewamanage,[4]
D. Hidas,[16] C. S. Hill,[10,c] D. Hirschbuehl,[26] A. Hocker,[17] S. Hou,[1] M. Houlden,[29] S.-C. Hsu,[9] B. T. Huffman,[41]
R. E. Hughes,[38] U. Husemann,[59] J. Huston,[35] J. Incandela,[10] G. Introzzi,[45] M. Iori,[50] A. Ivanov,[7] B. Iyutin,[32] E. James,[17]
B. Jayatilaka,[16] D. Jeans,[50] E. J. Jeon,[27] S. Jindariani,[18] W. Johnson,[7] M. Jones,[47] K. K. Joo,[27] S. Y. Jun,[12] J. E. Jung,[27]
T. R. Junk,[24] T. Kamon,[52] D. Kar,[18] P. E. Karchin,[57] Y. Kato,[40] R. Kephart,[17] U. Kerzel,[26] V. Khotilovich,[52] B. Kilminster,[38]
D. H. Kim,[27] H. S. Kim,[27] J. E. Kim,[27] M. J. Kim,[17] S. B. Kim,[27] S. H. Kim,[54] Y. K. Kim,[13] N. Kimura,[54] L. Kirsch,[6]
S. Klimenko,[18] M. Klute,[32] B. Knuteson,[32] B. R. Ko,[16] S. A. Koay,[10] K. Kondo,[56] D. J. Kong,[27] J. Konigsberg,[18]
A. Korytov,[18] A. V. Kotwal,[16] J. Kraus,[24] M. Kreps,[26] J. Kroll,[44] N. Krumnack,[4] M. Kruse,[16] V. Krutelyov,[10] T. Kubo,[54]
S. E. Kuhlmann,[2] T. Kuhr,[26] N. P. Kulkarni,[57] Y. Kusakabe,[56] S. Kwang,[13] A. T. Laasanen,[47] S. Lai,[33] S. Lami,[45]
S. Lammel,[17] M. Lancaster,[30] R. L. Lander,[7] K. Lannon,[38] A. Lath,[51] G. Latino,[45] I. Lazzizzera,[42] T. LeCompte,[2] J. Lee,[48]
J. Lee,[27] Y. J. Lee,[27] S. W. Lee,[52,q] R. Lefèvre,[20] N. Leonardo,[32] S. Leone,[45] S. Levy,[13] J. D. Lewis,[17] C. Lin,[59] C. S. Lin,[28]
J. Linacre,[41] M. Lindgren,[17] E. Lipeles,[9] A. Lister,[7] D. O. Litvintsev,[17] T. Liu,[17] N. S. Lockyer,[44] A. Loginov,[59] M. Loreti,[42]
L. Lovas,[14] R.-S. Lu,[1] D. Lucchesi,[42] J. Lueck,[26] C. Luci,[50] P. Lujan,[28] P. Lukens,[17] G. Lungu,[18] L. Lyons,[41] J. Lys,[28]
R. Lysak,[14] E. Lytken,[47] P. Mack,[26] D. MacQueen,[33] R. Madrak,[17] K. Maeshima,[17] K. Makhoul,[32] T. Maki,[23]
P. Maksimovic,[25] S. Malde,[41] S. Malik,[30] G. Manca,[29] A. Manousakis,[15,a] F. Margaroli,[47] C. Marino,[26] C. P. Marino,[24]
A. Martin,[59] M. Martin,[25] V. Martin,[21,j] M. Martínez,[3] R. Martínez-Ballarín,[31] T. Maruyama,[54] P. Mastrandrea,[50]
T. Masubuchi,[54] M. E. Mattson,[57] P. Mazzanti,[5] K. S. McFarland,[48] P. McIntyre,[52] R. McNulty,[29,i] A. Mehta,[29]
P. Mehtala,[23] S. Menzemer,[11,k] A. Menzione,[45] P. Merkel,[47] C. Mesropian,[49] A. Messina,[35] T. Miao,[17] N. Miladinovic,[6]
J. Miles,[32] R. Miller,[35] C. Mills,[22] M. Milnik,[26] A. Mitra,[1] G. Mitselmakher,[18] H. Miyake,[54] S. Moed,[22] N. Moggi,[5]
C. S. Moon,[27] R. Moore,[17] M. Morello,[45] P. Movilla Fernandez,[28] J. Mülmenstädt,[28] A. Mukherjee,[17] Th. Muller,[26]
R. Mumford,[25] P. Murat,[17] M. Mussini,[5] J. Nachtman,[17] Y. Nagai,[54] A. Nagano,[54] J. Naganoma,[56] K. Nakamura,[54]
I. Nakano,[39] A. Napier,[55] V. Necula,[16] C. Neu,[44] M. S. Neubauer,[24] J. Nielsen,[28,f] L. Nodulman,[2] M. Norman,[9]

O. Norniella,[24] E. Nurse,[30] S. H. Oh,[16] Y. D. Oh,[27] I. Oksuzian,[18] T. Okusawa,[40] R. Oldeman,[29] R. Orava,[23] K. Osterberg,[23] S. Pagan Griso,[42] C. Pagliarone,[45] E. Palencia,[17] V. Papadimitriou,[17] A. Papaikonomou,[26] A. A. Paramonov,[13] B. Parks,[38] S. Pashapour,[33] J. Patrick,[17] G. Pauletta,[53] M. Paulini,[12] C. Paus,[32] D. E. Pellett,[7] A. Penzo,[53] T. J. Phillips,[16] G. Piacentino,[45] J. Piedra,[43] L. Pinera,[18] K. Pitts,[24] C. Plager,[8] L. Pondrom,[58] X. Portell,[3] O. Poukhov,[15] N. Pounder,[41] F. Prakoshyn,[15] A. Pronko,[17] J. Proudfoot,[2] F. Ptohos,[17,h] G. Punzi,[45] J. Pursley,[58] J. Rademacker,[41,c] A. Rahaman,[46] V. Ramakrishnan,[58] N. Ranjan,[47] I. Redondo,[31] B. Reisert,[17] V. Rekovic,[36] P. Renton,[41] M. Rescigno,[50] S. Richter,[26] F. Rimondi,[5] L. Ristori,[45] A. Robson,[21] T. Rodrigo,[11] E. Rogers,[24] S. Rolli,[55] R. Roser,[17] M. Rossi,[53] R. Rossin,[10] P. Roy,[33] A. Ruiz,[11] J. Russ,[12] V. Rusu,[17] H. Saarikko,[23] A. Safonov,[52] W. K. Sakumoto,[48] G. Salamanna,[50] O. Saltó,[3] L. Santi,[53] S. Sarkar,[50] L. Sartori,[45] K. Sato,[17] A. Savoy-Navarro,[43] T. Scheidle,[26] P. Schlabach,[17] E. E. Schmidt,[17] M. A. Schmidt,[13] M. P. Schmidt,[59] M. Schmitt,[37] T. Schwarz,[7] L. Scodellaro,[11] A. L. Scott,[10] A. Scribano,[45] F. Scuri,[45] A. Sedov,[47] S. Seidel,[36] Y. Seiya,[40] A. Semenov,[15] L. Sexton-Kennedy,[17] A. Sfyria,[20] S. Z. Shalhout,[57] M. D. Shapiro,[28] T. Shears,[29] P. F. Shepard,[46] D. Sherman,[22] M. Shimojima,[54,n] M. Shochet,[13] Y. Shon,[58] I. Shreyber,[20] A. Sidoti,[45] P. Sinervo,[33] A. Sisakyan,[15] A. J. Slaughter,[17] J. Slaunwhite,[38] K. Sliwa,[55] J. R. Smith,[7] F. D. Snider,[17] R. Snihur,[33] M. Soderberg,[34] A. Soha,[7] S. Somalwar,[51] V. Sorin,[35] J. Spalding,[17] F. Spinella,[45] T. Spreitzer,[33] P. Squillacioti,[45] M. Stanitzki,[59] R. St. Denis,[21] B. Stelzer,[8] O. Stelzer-Chilton,[41] D. Stentz,[37] J. Strologas,[36] D. Stuart,[10] J. S. Suh,[27] A. Sukhanov,[18] H. Sun,[55] I. Suslov,[15] T. Suzuki,[54] A. Taffard,[24,e] R. Takashima,[39] Y. Takeuchi,[54] R. Tanaka,[39] M. Tecchio,[34] P. K. Teng,[1] K. Terashi,[49] J. Thom,[17,g] A. S. Thompson,[21] G. A. Thompson,[24] E. Thomson,[44] P. Tipton,[59] V. Tiwari,[12] S. Tkaczyk,[17] D. Toback,[52] S. Tokar,[14] K. Tollefson,[35] T. Tomura,[54] D. Tonelli,[17] S. Torre,[19] D. Torretta,[17] S. Tourneur,[43] W. Trischuk,[33] Y. Tu,[44] N. Turini,[45] F. Ukegawa,[54] S. Uozumi,[54] S. Vallecorsa,[20] N. van Remortel,[23] A. Varganov,[34] E. Vataga,[36] F. Vázquez,[18,l] G. Velev,[17] C. Vellidis,[45,a] V. Veszpremi,[47] M. Vidal,[31] R. Vidal,[17] I. Vila,[11] R. Vilar,[11] T. Vine,[30] M. Vogel,[36] I. Volobouev,[28,q] G. Volpi,[45] F. Würthwein,[9] P. Wagner,[44] R. G. Wagner,[2] R. L. Wagner,[17] J. Wagner-Kuhr,[26] W. Wagner,[26] T. Wakisaka,[40] R. Wallny,[8] S. M. Wang,[1] A. Warburton,[33] D. Waters,[30] M. Weinberger,[52] W. C. Wester III,[17] B. Whitehouse,[55] D. Whiteson,[44,e] A. B. Wicklund,[2] E. Wicklund,[17] G. Williams,[33] H. H. Williams,[44] P. Wilson,[17] B. L. Winer,[38] P. Wittich,[17,g] S. Wolbers,[17] C. Wolfe,[13] T. Wright,[34] X. Wu,[20] S. M. Wynne,[29] A. Yagil,[9] K. Yamamoto,[40] J. Yamaoka,[51] T. Yamashita,[39] C. Yang,[59] U. K. Yang,[13,m] Y. C. Yang,[27] W. M. Yao,[28] G. P. Yeh,[17] J. Yoh,[17] K. Yorita,[13] T. Yoshida,[40] G. B. Yu,[48] I. Yu,[27] S. S. Yu,[17] J. C. Yun,[17] L. Zanello,[50] A. Zanetti,[53] I. Zaw,[22] X. Zhang,[24] Y. Zheng,[8,b] and S. Zucchelli[5]

(CDF Collaboration)

[1]*Institute of Physics, Academia Sinica, Taipei, Taiwan 11529, Republic of China*
[2]*Argonne National Laboratory, Argonne, Illinois 60439, USA*
[3]*Institut de Fisica d'Altes Energies, Universitat Autonoma de Barcelona, E-08193, Bellaterra (Barcelona), Spain*
[4]*Baylor University, Waco, Texas 76798, USA*
[5]*Istituto Nazionale di Fisica Nucleare, University of Bologna, I-40127 Bologna, Italy*
[6]*Brandeis University, Waltham, Massachusetts 02254, USA*
[7]*University of California, Davis, Davis, California 95616, USA*
[8]*University of California, Los Angeles, Los Angeles, California 90024, USA*
[9]*University of California, San Diego, La Jolla, California 92093, USA*
[10]*University of California, Santa Barbara, Santa Barbara, California 93106, USA*
[11]*Instituto de Fisica de Cantabria, CSIC-University of Cantabria, 39005 Santander, Spain*
[12]*Carnegie Mellon University, Pittsburgh, Pennsylvania 15213, USA*
[13]*Enrico Fermi Institute, University of Chicago, Chicago, Illinois 60637, USA*
[14]*Comenius University, 842 48 Bratislava, Slovakia;*
Institute of Experimental Physics, 040 01 Kosice, Slovakia
[15]*Joint Institute for Nuclear Research, RU-141980 Dubna, Russia*
[16]*Duke University, Durham, North Carolina 27708*
[17]*Fermi National Accelerator Laboratory, Batavia, Illinois 60510, USA*
[18]*University of Florida, Gainesville, Florida 32611, USA*
[19]*Laboratori Nazionali di Frascati, Istituto Nazionale di Fisica Nucleare, I-00044 Frascati, Italy*
[20]*University of Geneva, CH-1211 Geneva 4, Switzerland*
[21]*Glasgow University, Glasgow G12 8QQ, United Kingdom*
[22]*Harvard University, Cambridge, Massachusetts 02138, USA*
[23]*Division of High Energy Physics, Department of Physics, University of Helsinki and Helsinki Institute of Physics,*
FIN-00014, Helsinki, Finland

[24]*University of Illinois, Urbana, Illinois 61801, USA*

[25]*The Johns Hopkins University, Baltimore, Maryland 21218, USA*

[26]*Institut für Experimentelle Kernphysik, Universität Karlsruhe, 76128 Karlsruhe, Germany*

[27]*Center for High Energy Physics: Kyungpook National University, Daegu 702-701, Korea;*
Seoul National University, Seoul 151-742, Korea;
Sungkyunkwan University, Suwon 440-746, Korea;
Korea Institute of Science and Technology Information, Daejeon, 305-806, Korea;
Chonnam National University, Gwangju, 500-757, Korea

[28]*Ernest Orlando Lawrence Berkeley National Laboratory, Berkeley, California 94720, USA*

[29]*University of Liverpool, Liverpool L69 7ZE, United Kingdom*

[30]*University College London, London WC1E 6BT, United Kingdom*

[31]*Centro de Investigaciones Energeticas Medioambientales y Tecnologicas, E-28040 Madrid, Spain*

[32]*Massachusetts Institute of Technology, Cambridge, Massachusetts 02139, USA*

[33]*Institute of Particle Physics: McGill University, Montréal, Canada H3A 2T8;*
and University of Toronto, Toronto, Canada M5S 1A7

[34]*University of Michigan, Ann Arbor, Michigan 48109, USA*

[35]*Michigan State University, East Lansing, Michigan 48824, USA*

[36]*University of New Mexico, Albuquerque, New Mexico 87131, USA*

[37]*Northwestern University, Evanston, Illinois 60208, USA*

[38]*The Ohio State University, Columbus, Ohio 43210, USA*

[39]*Okayama University, Okayama 700-8530, Japan*

[40]*Osaka City University, Osaka 588, Japan*

[41]*University of Oxford, Oxford OX1 3RH, United Kingdom*

[42]*University of Padova, Istituto Nazionale di Fisica Nucleare, Sezione di Padova-Trento, I-35131 Padova, Italy*

[43]*LPNHE, Universite Pierre et Marie Curie/IN2P3-CNRS, UMR7585, Paris, F-75252 France*

[44]*University of Pennsylvania, Philadelphia, Pennsylvania 19104, USA*

[45]*Istituto Nazionale di Fisica Nucleare Pisa, Universities of Pisa, Siena*
and Scuola Normale Superiore, I-56127 Pisa, Italy

[46]*University of Pittsburgh, Pittsburgh, Pennsylvania 15260, USA*

[47]*Purdue University, West Lafayette, Indiana 47907, USA*

[48]*University of Rochester, Rochester, New York 14627, USA*

[49]*The Rockefeller University, New York, New York 10021, USA*

[50]*Istituto Nazionale di Fisica Nucleare, Sezione di Roma 1, University of Rome "La Sapienza," I-00185 Roma, Italy*

[51]*Rutgers University, Piscataway, New Jersey 08855, USA*

[52]*Texas A&M University, College Station, Texas 77843, USA*

[53]*Istituto Nazionale di Fisica Nucleare, University of Trieste/Udine, Italy*

[54]*University of Tsukuba, Tsukuba, Ibaraki 305, Japan*

[55]*Tufts University, Medford, Massachusetts 02155, USA*

[56]*Waseda University, Tokyo 169, Japan*

[57]*Wayne State University, Detroit, Michigan 48201, USA*

[a]Visiting from University of Athens, 15784 Athens, Greece.

[b]Visiting from Chinese Academy of Sciences, Beijing 100864, China.

[c]Visiting from University of Bristol, Bristol BS8 1TL, United Kingdom.

[d]Visiting from University Libre de Bruxelles, B-1050 Brussels, Belgium.

[e]Visiting from University of California, Irvine, Irvine, CA 92697, USA.

[f]Visiting from University of California, Santa Cruz, Santa Cruz, CA 95064, USA.

[g]Visiting from Cornell University, Ithaca, NY 14853, USA.

[h]Visiting from University of Cyprus, Nicosia CY-1678, Cyprus.

[i]Visiting from University College Dublin, Dublin 4, Ireland.

[j]Visiting from University of Edinburgh, Edinburgh EH9 3JZ, United Kingdom.

[k]Visiting from University of Heidelberg, D-69120 Heidelberg, Germany.

[l]Visiting from Universidad Iberoamericana, Mexico D.F., Mexico.

[m]Visiting from University of Manchester, Manchester M13 9PL, England.

[n]Visiting from Nagasaki Institute of Applied Science, Nagasaki, Japan.

[o]Visiting from University de Oviedo, E-33007 Oviedo, Spain.

[p]Visiting from Queen Mary, University of London, London, E1 4NS, England.

[q]Visiting from Texas Tech University, Lubbock, TX 79409, USA.

[r]Visiting from IFIC(CSIC-Universitat de Valencia), 46071 Valencia, Spain.

[58]*University of Wisconsin, Madison, Wisconsin 53706, USA*
[59]*Yale University, New Haven, Connecticut 06520, USA*

We present the first observation and cross section measurement of exclusive dijet production in $\bar{p}p$ interactions, $\bar{p}p \to \bar{p} + \text{dijet} + p$. Using a data sample of 310 pb^{-1} collected by the Run II Collider Detector at Fermilab at $\sqrt{s} = 1.96$ TeV, exclusive cross sections for events with two jets of transverse energy $E_T^{\text{jet}} \geq 10$ GeV have been measured as a function of minimum E_T^{jet}. The exclusive signal is extracted from fits to data distributions based on Monte Carlo simulations of expected dijet signal and background shapes. The simulated background distribution shapes are checked in a study of a largely independent data sample of 200 pb^{-1} of b-tagged jet events, where exclusive dijet production is expected to be suppressed by the $J_z = 0$ total angular momentum selection rule. Results obtained are compared with theoretical expectations, and implications for exclusive Higgs boson production at the pp Large Hadron Collider at $\sqrt{s} = 14$ TeV are discussed.

I. INTRODUCTION

Exclusive dijet production in $\bar{p}p$ collisions is a process in which both the antiproton and proton escape the interaction point (IP) intact and a two-jet system is centrally produced:

$$\bar{p} + p \to \bar{p}' + (\text{jet}_1 + \text{jet}_2) + p'. \quad (1)$$

This process is a particular case of dijet production in double Pomeron exchange (DPE), a diffractive process in which the antiproton and proton suffer a small fractional momentum loss, and a system X containing the jets is produced,

$$\bar{p} + p \to [\bar{p}' + \mathbb{P}_{\bar{p}}] + [p' + \mathbb{P}_p] \to \bar{p}' + X + p', \quad (2)$$

where $\mathbb{P}$ designates a Pomeron, defined as an exchange consisting of a colorless combination of gluons and/or quarks carrying the quantum numbers of the vacuum.

In a particlelike Pomeron picture (e.g. see [1]), the system X may be thought of as being produced by the collision of two Pomerons, $\mathbb{P}_{\bar{p}}$ and $\mathbb{P}_p$,

$$\mathbb{P}_{\bar{p}} + \mathbb{P}_p \to X \Rightarrow Y_{\mathbb{P}/\bar{p}} + (\text{jet}_1 + \text{jet}_2) + Y_{\mathbb{P}/p}, \quad (3)$$

where in addition to the jets the final state generally contains Pomeron remnants designated by $Y_{\mathbb{P}/\bar{p}}$ and $Y_{\mathbb{P}/p}$. Dijet production in DPE is a subprocess to dijet production in single diffraction (SD) dissociation, where only the antiproton (proton) survives while the proton (antiproton) dissociates. Schematic diagrams for SD and DPE dijet production are shown in Fig. 1 along with event topologies in pseudorapidity space (from Ref. [2]). In SD, the escaping $\bar{p}$ is adjacent to a rapidity gap, defined as a region of pseudorapidity devoid of particles [3]. A rapidity gap arises because the Pomeron exchanged in a diffractive process is a colorless object of effective spin $J \geq 1$ and carries the quantum numbers of the vacuum. In DPE, two such rapidity gaps are present.

Dijet production in DPE may occur as an exclusive process [4] with only the jets in the final state and no Pomeron remnants, either due to a fluctuation of the Pomeron remnants down to zero or with a much higher cross section in models in which the Pomeron is treated as a parton and the dijet system is produced in a $2 \to 2$ process analogous to $\gamma\gamma \to \text{jet} + \text{jet}$ [5].

In a special case exclusive dijets may be produced through an intermediate state of a Higgs boson decaying into $\bar{b}b$:

$$\mathbb{P}_{\bar{p}} + \mathbb{P}_p \to H^0 \to (\bar{b} \to \text{jet}_1) + (b \to \text{jet}_2). \quad (4)$$

Exclusive production may also occur through a t-channel color-singlet two gluon exchange at leading order (LO) in perturbative quantum chromo-dynamics (QCD), as shown schematically in Fig. 2(a), where one of the two gluons takes part in the hard scattering that produces the jets, while the other neutralizes the color flow [6]. A similar diagram, Fig. 2(b), is used in [6] to calculate exclusive Higgs boson production.

Exclusive dijet production has never previously been observed in hadronic collisions. In addition to providing information on QCD aspects of vacuum quantum number exchange, there is currently intense interest in using mea-
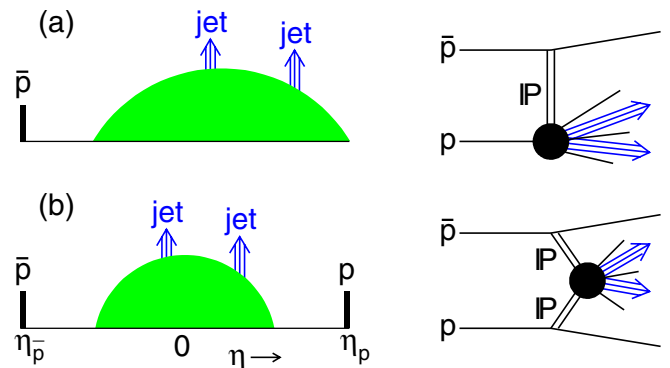

FIG. 1 (color online).   Illustration of event topologies in pseudorapidity, η, and associated Pomeron exchange diagrams for dijet production in (a) single diffraction and (b) double Pomeron exchange. The shaded areas on the left side represent "underlying event" particles not associated with the jets (from Ref. [2]).
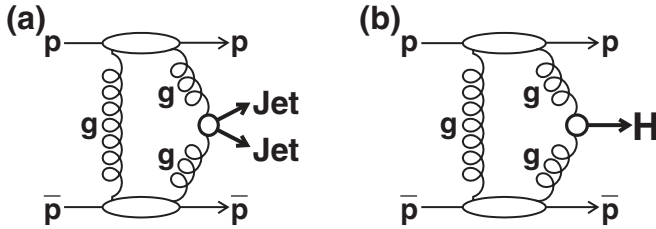
FIG. 2. Leading order diagrams for (a) exclusive dijet and (b) exclusive Higgs boson production in $\bar{p}p$ collisions.

sured exclusive dijet production cross sections to calibrate theoretical predictions for exclusive Higgs boson production at the Large Hadron Collider (LHC). Such predictions are generally hampered by large uncertainties due to non-perturbative suppression effects associated with the rapidity gap survival probability. As these effects are common to exclusive dijet and Higgs boson production mechanisms, dijet production potentially provides a ``standard candle'' process against which to calibrate the theoretical models [6,7].

In Run I (1992–96) of the Fermilab Tevatron $\bar{p}p$ collider operating at 1.8 TeV, the Collider Detector at Fermilab (CDF) collaboration made the first observation of dijet production by DPE [2] using an inclusive sample of SD events, $\bar{p}p \rightarrow \bar{p}'X$, collected by triggering on a $\bar{p}$ detected in a forward Roman pot spectrometer (RPS). DPE dijet events were selected from this sample by requiring, in addition to the $\bar{p}$ detected by the RPS, the presence of two jets with transverse energy $E_T > 7$ GeV and a rapidity gap in the outgoing proton direction in the range $2.4 < \eta < 5.9$ [8]. In the resulting sample of 132 inclusive DPE dijet events, no evidence for exclusive dijet production was found, setting a 95% confidence level upper limit of 3.7 nb on the exclusive production cross section. At that time, theoretical estimates of this cross section ranged from $\sim 10^3$ larger [9] to a few times smaller [6] than our measured upper bound. More data were clearly needed to observe an exclusive dijet signal and test theoretical predictions of kinematical properties and production rates.

In Run II-A (2001–06), with the Tevatron providing $\bar{p}p$ collisions at $\sqrt{s} = 1.96$ TeV, two high statistics data samples of DPE dijet events were collected by the upgraded CDF II detector: one of inclusive dijets, and another largely independent sample of b-quark jets. The analysis of these data is the subject of this paper. The results obtained provide the first evidence for exclusive dijet production in $\bar{p}p$ collisions.

The paper is organized as follows. In Sec. II, we present the strategy employed to control the experimental issues involved in searching for an exclusive dijet signal. We then describe the detector (Sec. III), the data samples and event selection (Sec. IV), the data analysis for inclusive DPE (Sec. V) and exclusive dijet production (Sec. VI), results and comparisons with theoretical predictions (Sec. VII),

and background shape studies using heavy flavor quark jets (Sec. VIII). Implications for exclusive Higgs boson production at the Large Hadron Collider are discussed in Sec. IX, and conclusions are presented in Sec. X.

II. STRATEGY

Exclusive dijet production is characterized by two jets in the final state and no additional final state particles except for the escaping forward proton and antiproton. Therefore, searching for exclusive dijet production would ideally require a full acceptance detector in which all final state particles are detected, their vector momenta are measured, the correct particles are assigned to each jet, and ``exclusivity'' is certified by the absence of any additional final state particle(s). Assigning particles to a jet is a formidable challenge because the detector threshold settings used to reduce noise may inadvertently either eliminate particles with energies below threshold or else result in noise being counted as additional particles if the thresholds are set too low. To meet this challenge, we developed a strategy incorporating detector design, online triggers, data sets used for background estimates, and an analysis technique sensitive to an exclusive signal but relatively immune to the above mentioned effects.

The exclusive signal is extracted using the ``dijet mass fraction'' method developed in our Run I data analysis. From the energies and momenta of the jets in an event, the ratio $R_{jj} \equiv M_{jj}/M_X$ of the dijet mass M_{jj} to the total mass M_X of the final state (excluding the $\bar{p}$ and p) is formed and used to discriminate between the signal of exclusive dijets, expected to appear at $R_{jj} = 1$, and the background of inclusive DPE dijets, expected to have a continuous distribution concentrated at lower R_{jj} values. Because of smearing effects in the measurement of E_T^{jet} and η^{jet} and gluon radiation from the jets the exclusive dijet peak is broadened and shifts to lower R_{jj} values. The exclusive signal is therefore obtained by a fit of the R_{jj} distribution to expected signal and background shapes generated by Monte Carlo (MC) simulations. The background shape used is checked with an event sample of heavy quark flavor dijets, for which exclusive production is expected to be suppressed in LO QCD by the $J_z = 0$ selection rule of the hard scattered di-gluon system, where J_z is the projection of the total angular momentum of the system along the beam direction [10].

III. DETECTOR

The CDF II detector, shown schematically in Fig. 3, is described in detail elsewhere [11]. The detector components most relevant for this analysis are the charged particle tracking system, the central and plug calorimeters, and a set of detectors instrumented in the forward pseudorapidity region. The CDF tracking system consists of a silicon vertex detector (SVX II) [12], composed of
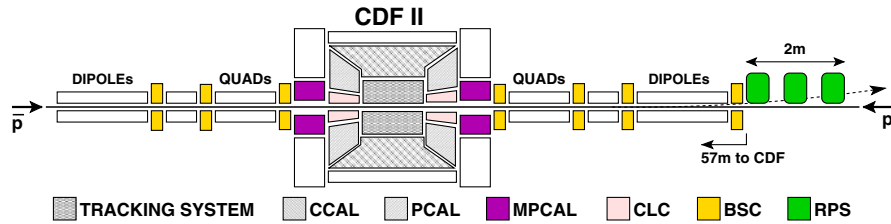
FIG. 3 (color online).   Schematic drawing (not to scale) of the CDF II detector.

double-sided microstrip silicon sensors arranged in five cylindrical shells of radii between 2.5 and 10.6 cm, and an open-cell drift chamber [13] of 96 layers organized in 8 superlayers with alternating structures of axial and $\pm 2°$ stereo readout within a radial range between 40 and 137 cm. Surrounding the tracking detectors is a superconducting solenoid, which provides a magnetic field of 1.4 T. Calorimeters located outside the solenoid are physically divided into a central calorimeter (CCAL) [14,15], covering the pseudorapidity range $|\eta| < 1.1$, and a plug calorimeter (PCAL) [16], covering the region $1.1 < |\eta| < 3.6$. These calorimeters are segmented into projective towers of granularity $\Delta\eta \times \Delta\phi \approx 0.1 \times 15°$.

The forward detectors [17], which extend the coverage into the η region beyond 3.6, consist of the MiniPlug calorimeters (MPCAL) [18], the beam shower counters (BSC), a Roman pot spectrometer (RPS), and a system of Cherenkov luminosity counters (CLC). The MiniPlug calorimeters, shown schematically in Fig. 4, are designed to measure the energy and lateral position of particles in the region $3.6 < |\eta| < 5.2$. They consist of alternating lead plates and liquid scintillator layers perpendicular to the

beam, which are read out by wavelength shifting fibers that pass through holes drilled through the plates parallel to the beam direction. Each MiniPlug is 32 (1.3) radiation (interaction) lengths deep. The BSC are scintillation counters surrounding the beam pipe at three (four) different locations on the outgoing proton (antiproton) side of the CDF II detector. Covering the range $5.4 < |\eta| < 5.9$ is the BSC1 system, which is closest to the interaction point and is used for measuring beam losses and for triggering on events with forward rapidity gaps. Lead plates of thickness 1.7 radiation lengths precede each BSC1 counter to convert γ rays to e^+e^- pairs to be detected by the scintillators. The RPS, located at ~ 57 m downstream in the antiproton beam direction, consists of three Roman pot stations, each containing a scintillation counter used for triggering on the $\bar{p}$, and a scintillation fiber tracking detector for measuring the position and angle of the detected $\bar{p}$. The CLC [19], covering the range $3.7 < |\eta| < 4.7$, which substantially overlaps the MiniPlug coverage, are normally used in CDF to measure the number of inelastic $\bar{p}p$ collisions per bunch crossing and thereby the luminosity. In this analysis, they are also used to refine the rapidity gap definition by detecting charged particles that might penetrate a MiniPlug without interacting and thus produce too small a pulse height to be detected over the MiniPlug tower thresholds used.

IV. DATA SAMPLES AND EVENT SELECTION

Three data samples are used in this analysis, referred to as the DPE, SD, and nondiffractive (ND) event samples. The exclusive signal is derived from the DPE event sample, while the SD and ND samples are used for evaluating backgrounds. The total integrated luminosity of the DPE sample is 312.5 ± 18.7 pb^{-1}.

The following trigger definitions are used:
- (a) J5: a single CCAL or PCAL calorimeter trigger tower of $E_T > 5$ GeV.
- (b) RPS: a triple coincidence among the three RPS trigger counters in time with a $\bar{p}$ gate.
- (c) $\overline{\text{BSC1}_p}$: a BSC1 veto on the outgoing proton side.

The three event samples were collected with the following triggers:

$$\text{ND} \equiv \text{J5}, \quad \text{SD} \equiv \text{J5} \cdot \text{RPS}, \quad \text{DPE} \equiv \text{J5} \cdot \text{RPS} \cdot \overline{\text{BSC1}_p}.$$

The DPE events, from which cross sections are calculated, were sampled at a rate of one out of five events to
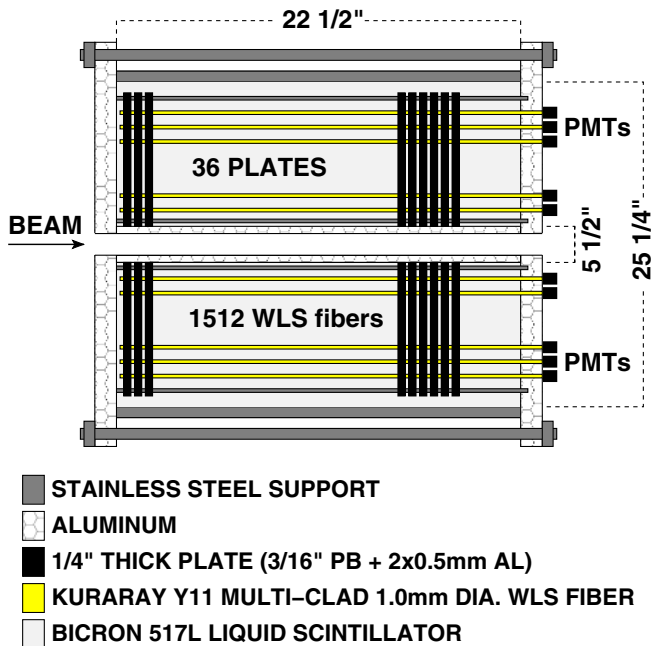

FIG. 4 (color online).   Schematic cross sectional view of one of the two forward MiniPlug calorimeters installed in CDF II.

accommodate the trigger bandwidth. In the above sample definition, ND events include SD and DPE contributions, and SD events include DPE ones. This results in a "contamination" of background distributions by signal events, which is taken into account in the data analysis.

The selection cuts used in the data analysis include:

(a) VTX cut (ND, SD, and DPE): No more than one reconstructed primary vertex within $|z| < 60$ cm, imposed to reduce the number of overlap events occurring during the same beam-beam crossing at the IP.

(b) RPST cut (SD and DPE): RPS trigger counter pulse height cut, imposed to reject "splash" triggers caused by particles hitting the beam pipe in the vicinity of the RPS and spraying the RPST counters with secondary particles.

(c) Jet cut (ND, SD, and DPE): Events are required to have at least two jets with transverse energy $E_T^{\text{jet}} > 10$ GeV within $|\eta| < 2.5$.

The transverse energy of a jet is defined as the sum $E_T^{\text{jet}} \equiv \Sigma_i E_i \sin(\theta_i)$ of all calorimeter towers at polar angles θ_i within the jet cone. Jets are reconstructed with the midpoint algorithm [20], which is an improved iterative cone clustering algorithm, using a cone radius of 0.7 in η-ϕ space and based on calorimeter towers with E_T above 100 MeV. The E_T of a jet is defined as the sum of the E_T values of the clustered calorimeter towers. The jet E_T is corrected for the relative response of the calorimeters and for the absolute energy scale.

The above selection cuts define the DPE data sample (DPE) and are summarized below:

$$\text{DPE sample: J5} \cdot \text{RPS} \cdot \overline{\text{BSC1}_p} \cdot \text{VTX} \cdot \text{RPST} \cdot \text{JET.} \tag{5}$$

The DPE data sample consists of 415 688 events.

Backgrounds in the DPE event sample fall into two general categories: (i) SD dijet events, in which the $\overline{\text{BSC1}_p}$ requirement is fulfilled by a downward BSC1_p multiplicity fluctuation to zero, and (ii) overlaps between a ND J5 trigger and a RPS trigger provided by either a low mass soft SD event that has no reconstructed vertex or by a scattered beam halo or ND event particle. To reduce these backgrounds, two more requirements are imposed on the data: a large rapidity gap on the outgoing proton direction, LRG_p, and passing the $\xi_{\bar{p}}^X$ cut defined below.

(a) LRG_p: This requirement is implemented by demanding zero multiplicities in MPCAL_p and CLC_p, $N_{\text{MPCAL}}^p = N_{\text{CLC}}^p = 0$, added to the trigger requirement of $\text{BSC1}_p = 0$. The LRG_p approximately covers the range of $3.6 < \eta < 5.9$. This selection cut enriches the DPE event sample in exclusive events by removing nonexclusive backgrounds. Although there is a substantial overlap between the pseudorapidity regions covered by

MPCAL_p and CLC_p, the requirements of $\text{MPCAL}_p = 0$ and $\text{CLC}_p = 0$ are nevertheless complementary, as the two systems detect hadrons and electromagnetic particles with different efficiencies.

(b) $\xi_{\bar{p}}^X$ cut: $0.01 < \xi_{\bar{p}}^X < 0.12$.

In the high instantaneous luminosity environment of Run II, multiple $\bar{p}p$ interactions occurring in the same beam-beam bunch crossing may result in overlap events consisting of a ND dijet event overlapped by a soft SD event with a leading $\bar{p}$ triggering by the RPS. These events, which are a background to both DPE and SD dijet events, can be well separated from diffractively produced dijet events using the variable $\xi_{\bar{p}}^X$, defined as

$$\xi_{\bar{p}}^X = \frac{1}{\sqrt{s}} \sum_{i=1}^{N_{\text{tower}}} (E_T^i e^{-\eta^i}), \tag{6}$$

where the sum is carried out over all calorimeter towers with $E_T > 100$ MeV for CCAL and PCAL, and $E_T > 20$ MeV for MPCAL. The tower E_T and η are measured with respect to the primary vertex position. The variable $\xi_{\bar{p}}^X$ represents the fractional longitudinal momentum loss of the $\bar{p}$ measured using calorimeter information. For events with a gap on the $\bar{p}$ side, $\xi_{\bar{p}}^X$ is calibrated by comparing data with Monte Carlo generated events. Calibrated $\xi_{\bar{p}}^X$ values were found to be in good agreement with values of $\xi_{\bar{p}}$ measured by the RPS, $\xi_{\bar{p}}^{\text{RPS}}$. On the proton side where there is no RPS, ξ_p^X is obtained from calorimeter information using Eq. (6) in which $-\eta$ in the exponent is changed to $+\eta$ and is calibrated using the MC technique that was validated by the comparison with RPS data on the $\bar{p}$ side. Figure 5(a) shows $\xi_{\bar{p}}^X$ distributions for events of the DPE event sample selected with the LRG_p requirement. The events in the peak at $\xi_{\bar{p}}^X \sim 0.05$ are dominated by DPE dijets, while the broad peak around $\xi_{\bar{p}}^X \sim 0.3$ are residual overlap ND dijet events for which the LRG_p is caused by downward multiplicity fluctuations.

In this analysis, we use the DPE dominated events in the range $0.01 < \xi_{\bar{p}}^X < 0.12$. The same $\xi_{\bar{p}}^X$ requirement is used in selecting the SD event sample. Figure 5(b) shows the MPCAL hit multiplicity, N_{MP}^p, vs BSC1 hit counter multiplicity, N_{BSC1}^p, for the SD event sample. The majority of the events have $5 < N_{\text{MP}}^p < 10$ and $N_{\text{BSC1}}^p \geq 3$, but there are also some events with $N_{\text{BSC1}}^p = N_{\text{MP}}^p = 0$, which are due to DPE events in the SD event sample efficiently passing the $\overline{\text{BSC1}_p}$ trigger requirement.

The above trigger and offline selection requirements define the inclusive DPE event sample (IDPE).

$$\text{IDPE sample: DPE} \cdot \text{LRG}_p \cdot \xi_{\bar{p}}^X. \tag{7}$$

The IDPE sample contains 20 414 events.

In Fig. 6, we compare distributions of the mean dijet transverse energy, $E_T^* = (E_T^{\text{jet1}} + E_T^{\text{jet2}})/2$, mean pseudorapidity, $\eta^* = (\eta_{\text{jet1}} + \eta_{\text{jet2}})/2$, and azimuthal angle differ-
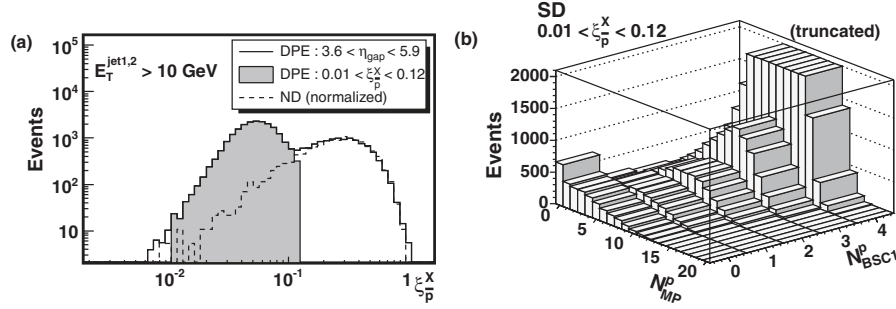
FIG. 5.   (a) $\xi_{\bar{p}}^X$ distribution of DPE events passing the LRG$_p$ requirement (solid histogram), with the shaded area representing events in the region $0.01 < \xi_{\bar{p}}^X < 0.12$; the dashed histogram shows the $\xi_{\bar{p}}^X$ distribution for ND events passing the same LRG$_p$ requirement and normalized to the solid histogram in the plateau region of $0.22 < \xi_{\bar{p}}^X < 0.50$; (b) MPCAL hit multiplicity, N_{MP}^p, vs BSC1$_p$ hit counter multiplicity, N_{BSC1}^p, in SD events with $0.01 < \xi_{\bar{p}}^X < 0.12$.

ence, $\Delta\phi = |\phi_{\text{jet1}} - \phi_{\text{jet2}}|$, for IDPE (points), SD (solid histogram), and ND (dashed histogram) events. All distributions are normalized to unit area. The IDPE, SD, and ND distributions exhibit the following features: (a) the E_T^* distributions for IDPE, SD, and ND events are similar at low E_T^*, but reach larger E_T^* values for SD and ND events due to the higher c.m.s. energies of $\mathbb{P}$-p and $\bar{p}p$ collisions relative to $\mathbb{P}$-$\mathbb{P}$ collisions; (b) the ND η^* distribution is symmetric about $\eta^* = 0$, as expected, and the DPE distribution is approximately symmetric as the jets are produced in collisions between two Pomerons of approximately equal momentum (due to the approximately equal gap size on the p and $\bar{p}$ sides), while the SD distribution is boosted toward positive η^* (outgoing p direction) due to the jets being produced in collisions between a proton carrying the beam momentum, p_0, and a Pomeron of

much smaller momentum, $\xi_{\bar{p}} p_0$; and (c) the jets are more back-to-back in SD than in ND events, and even more so in IDPE events, due to less gluon radiation being emitted in events where colorless Pomerons are exchanged.

V. INCLUSIVE DPE DIJET PRODUCTION

The cross section for inclusive DPE dijet production is obtained from the IDPE event sample using the expression

$$\sigma_{\text{DPE}}^{\text{incl}} = \frac{N_{\text{DPE}}^{jj}(1 - F_{\text{BG}})}{L \cdot \epsilon}, \qquad (8)$$

where N_{DPE}^{jj} is the number of DPE dijet events corrected for losses due to multiple interactions and for smearing effects on E_T^{jet} due to the detector resolution, F_{BG} is the non-DPE
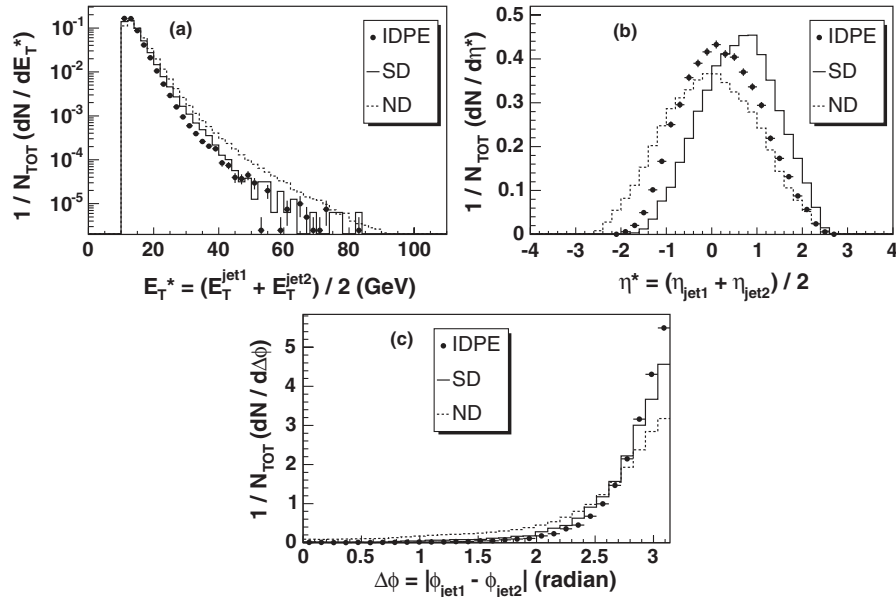

FIG. 6.   (a) Mean E_T, (b) mean η of the two leading jets, and (c) azimuthal angle difference between the two leading jets of $E_T > 10$ GeV in IDPE (circles), SD (solid histograms), and ND (dashed histograms) dijet events.

background fraction, L is the integrated luminosity, and ϵ is the total event selection efficiency including detector acceptance. Details are provided below.

A. Non-DPE background events

There are two sources of non-DPE background events in the IDPE event sample underneath the DPE peak at $0.01 < \xi_{\bar{p}}^X < 0.12$ shown in Fig. 5(a): one due to ND dijet events and the other due to SD ones. In both cases, the LRG_p requirement of $N_{BSC1}^p = N_{MP}^p = N_{CLC}^p = 0$ is satisfied by downward multiplicity fluctuations.

Nondiffractive background. The ND background is caused by the RPS being triggered either by a real anti-proton from an overlapping soft SD event or by a particle originating in beam-pipe or beam-gas interactions. This background is estimated from the $\xi_{\bar{p}}^X$ distribution of ND dijet events with $N_{BSC1}^p = N_{MP}^p = N_{CLC}^p = 0$ normalized to the $\xi_{\bar{p}}^X$ distribution of DPE events in the region $0.22 < \xi_{\bar{p}}^X < 0.50$, which is dominated by ND events. The DPE (normalized ND) $\xi_{\bar{p}}^X$ distribution is shown in Fig. 5(a) as a solid (dashed) histogram. Integrating the ND distribution over the range $0.01 < \xi_{\bar{p}}^X < 0.12$, we obtain the fraction of ND dijet background in the IDPE event sample to be $F_{BG}^{ND} = 13.3 \pm 0.2\%$.

Single diffractive background. The SD background is estimated by examining the correlation between $N_{BSC1}^p + N_{MP}^p$ and N_{CLC}^p in the SD data sample. Figure 7(a) shows the distribution of $N_{BSC1}^p + N_{MP}^p$ versus N_{CLC}^p for SD dijet events with $0.01 < \xi_{\bar{p}}^X < 0.12$. The multiplicity along the diagonal, N_{diag}, defined by $N_{BSC1}^p + N_{MP}^p = N_{CLC}^p$, is well fitted with a linear function in the region $2 \le N_{diag} \le 14$, as shown in Fig. 7(b). The diagonal distribution is used because it monotonically decreases as $N_{diag} \to 0$ providing the least background under the peak. Extrapolating the fit to the bin with $N_{BSC1}^p = N_{MP}^p = N_{CLC}^p = 0$ yields a SD background fraction of $F_{00} = 24 \pm 4\%$. After correcting

for a ND content of 42% in the SD data, estimated by applying the method used in evaluating F_{BG}^{ND}, we obtain a single diffractive background fraction of $F_{BG}^{SD} = F_{00} \times (1 - 0.42) = 14 \pm 3\%$.

B. Corrections for multiple interactions

Multiple interactions in the same beam-beam crossing may produce additional events which overlap the DPE event and cause it to fail the event selection requirements by contributing extra event vertices and/or by spoiling the rapidity gap on the proton side. Corrections for DPE event losses due to multiple interactions are considered separately for overlapping events with one or more reconstructed vertices, and for overlapping events which do not have a vertex but nevertheless spoil the LRG_p. The latter also account for LRG_p losses due to beam background and/or detector noise.

Overlap events with a reconstructed vertex. The average number of inelastic $\bar{p}p$ interactions per bunch crossing is given by $\bar{n}_i = \mathcal{L}_i \cdot \sigma_{inel}/f_0$, where $\mathcal{L}_i$ is the instantaneous luminosity, σ_{inel} the inelastic interaction cross section, and f_0 the Tevatron bunch crossing frequency of 1.674 MHz. The average number of $\bar{p}p$ interactions which have a vertex, $\bar{n}_i^{vtx}$, is obtained by replacing σ_{inel} with σ_{inel}^{vtx}, the cross section of $\bar{p}p$ interactions with a vertex. From Poisson statistics, the probability that no $\bar{p}p$ interaction producing a vertex occurs in a beam-beam bunch crossing is given by $P(0) = \exp(-\bar{n}_i^{vtx})$. The number of observed DPE events, N_{DPE}, corrected for losses due to multiple interactions that yield overlap events with a vertex, N_{DPE}^{corr}, is obtained by weighting every event by $P(0)^{-1}$ and summing up over all DPE events: $N_{DPE}^{corr} = \sum_{i=1}^{N_{DPE}} \exp(\bar{n}_i^{vtx})$.

The value of σ_{inel}^{vtx}, which is needed for evaluating $\bar{n}_i^{vtx}$, is obtained from an analysis of the fraction of events with one or more reconstructed vertices contained in a sample of zero-bias events collected by triggering on beam-beam crossings during the same time period in which the DPE
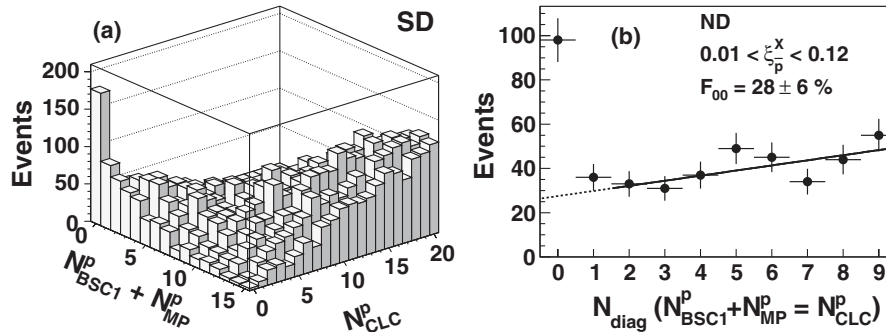

FIG. 7. (a) Sum of the BSC1 hit counter multiplicity and MPCAL hit multiplicity, $N_{BSC1}^p + N_{MP}^p$, versus CLC hit multiplicity, N_{CLC}^p, in SD events with dijets of $E_T^{jet1,2} > 10$ GeV and $0.01 < \xi_{\bar{p}}^X < 0.12$; (b) multiplicity distribution along the diagonal line in the left plot, N_{diag}, defined by $N_{BSC1}^p + N_{MP}^p = N_{CLC}^p$, with the solid line representing a linear fit in the region $2 \le N_{diag} \le 9$, and the dashed line the extrapolation of the fit to the $N_{diag} = 0$ bin.

sample was taken. The zero-bias sample is split into small subsamples corresponding to different time slots of data-taking to account for changes in beam and detector conditions, and the fraction of events with ≥ 1 vertex as a function of instantaneous luminosity for each subsample is fit to the expected fraction given by $1 - \mathrm{P}(0) = 1 - \exp(-\mathcal{L}_i \cdot \sigma_{\mathrm{inel}}^{\mathrm{vtx}}/f_0)$ with $\sigma_{\mathrm{inel}}^{\mathrm{vtx}}$ as a free parameter. The average value obtained from the fits is $\sigma_{\mathrm{inel}}^{\mathrm{vtx}} = 30.3 \pm 1.5(\mathrm{syst})$ mb, where the uncertainty is evaluated from the variations observed among the different subsamples. Using this value, we obtain $\mathrm{N}_{\mathrm{DPE}}^{\mathrm{corr}} = 189\,317 \pm 1325$ events for the IDPE sample. The ± 1.5 mb uncertainty in $\sigma_{\mathrm{inel}}^{\mathrm{vtx}}$ leads to an uncertainty of $\sim 2\%$ on $\mathrm{N}_{\mathrm{DPE}}^{\mathrm{corr}}$, which is negligibly small compared to other uncertainties discussed below.

Overlap events with no reconstructed vertex. The rapidity gap of DPE events remaining after rejecting events with more than one vertex could be further spoiled by the presence of additional soft $\bar{p}p$ interactions with no reconstructed vertex, by beam background, or by detector noise. The correction for these effects is obtained from the same zero-bias samples by selecting events with no reconstructed vertex and evaluating the fraction $\mathrm{F}_{\mathrm{gap}}$ of events with LRG_p. The correction factor, $\mathrm{F}_{\mathrm{gap}}^{-1}$, evaluated for bins of different instantaneous luminosity and data taking time, is then applied to $\mathrm{N}_{\mathrm{DPE}}^{\mathrm{corr}}$ for the same instantaneous luminosity and time bins. Within the instantaneous luminosity range of $10^{31} < \mathcal{L}_i < 4 \times 10^{31}$ cm^{-2} s^{-1} of our DPE data sample, $\mathrm{F}_{\mathrm{gap}}$ varies between 70% and 30%.

C. Event selection efficiency

Jet selection efficiency. The trigger efficiency for jets with a calorimeter trigger tower of $E_T > 5$ GeV is obtained from a sample of minimum-bias (MB) events triggered only on a CLC coincidence between the two sides of the detector. The E_T^{jet} and η^{jet} are reconstructed using the same algorithm as that used in the analysis of the IDPE dijet event sample. For MB events that contain a calorimeter trigger tower of $E_T^{\mathrm{tower}} > 5$ GeV, jets are selected if the trigger tower is contained within the $\Delta\eta$-$\Delta\phi$ cone of the jets. The trigger efficiency per jet is determined in bins of E_T^{jet} and η^{jet} as the ratio of the number of jets containing a trigger tower of $E_T^{\mathrm{tower}} > 5$ GeV to the total number of jets in all MB events. The single tower trigger efficiency for a given DPE dijet event, ϵ_{ST}, is derived from the efficiency per jet, the number of jets in the event, and the E_T and η values of each jet. The DPE data are corrected for the trigger efficiency by assigning a weight of ϵ_{ST}^{-1} to each event.

RPS trigger efficiency. The efficiency of triggering on a leading antiproton in the RPS trigger counters may be expressed as the product of the trigger counter acceptance, A_{RPS}, and the RPS detector efficiency, ϵ_{RPS}. The latter can be further factorized into two terms: the efficiency for finding the antiproton hits, $\epsilon_{\mathrm{RPS}h}$, and the efficiency of

the hit signals passing the trigger requirement, $\epsilon_{\mathrm{RPS}t}$. From a study of trigger counter signals produced by particles reconstructed as single tracks using a zero-bias event sample, we obtain $\epsilon_{\mathrm{RPS}h} = 97 \pm 1\%$. Using zero-bias events with signals in the trigger counters consistent with the response expected for minimum ionizing particles, $\epsilon_{\mathrm{RPS}t}$ is found to be unity. The trigger counter acceptance is obtained from a simulation of SD events using the beam transport matrix to carry the recoil $\bar{p}$ from the IP to the RPS detectors. The total RPS acceptance for DPE dijet events is obtained from the expression

$$A_{\mathrm{RPS}}^{\mathrm{total}} = \frac{N_{\mathrm{DPE}}}{\sum_{i=1}^{N_{\mathrm{DPE}}} A_{\mathrm{RPS}}(\xi_{\bar{p}_i}^{\mathrm{RPS}}, |t_{\bar{p}_i}^{\mathrm{RPS}}|)^{-1}}, \qquad (9)$$

where $t_{\bar{p}}^{\mathrm{RPS}}$ is the four momentum transfer squared measured by the RPS and N_{DPE} the total number of DPE dijet events. For the events collected in our data taking period we obtain $A_{\mathrm{RPS}}^{\mathrm{total}} = 78.4 \pm 0.3(\mathrm{stat.})\%$.

$\xi_{\bar{p}}^X$ cut efficiency. The requirement of $0.01 < \xi_{\bar{p}}^X < 0.12$ is used as a preselection cut to reduce ND dijet background due to superimposed $\bar{p}p$ interactions. However, this cut also removes some DPE events. The efficiency for DPE events retained by this requirement is obtained from the $\xi_{\bar{p}}^X$ distributions of the DPE and ND dijet events shown in Fig. 5(a) and used in Sec. VA to estimate the ND dijet background fraction in the IDPE data. Subtracting the normalized ND from the DPE events and evaluating the ratio of events within $0.01 < \xi_{\bar{p}}^X < 0.12$ to the total number of events yields an efficiency of $98.5 \pm 0.2\%$. The deficit of this efficiency with respect to unity is due to fluctuations and calorimeter resolution effects causing a small fraction of events to migrate outside the selected $\xi_{\bar{p}}^X$ range.

Single vertex cut efficiency. The single vertex requirement (VTX cut), which is imposed to reject events with multiple interactions, also rejects single interaction events with extra misidentified vertices resulting from ambiguities in track reconstruction. Comparing the number of IDPE events before and after imposing this requirement, we obtain a single vertex cut efficiency of $\epsilon_{1\mathrm{vtx}} = 98 \pm 1\%$. Using a similar method, the efficiency of the requirement of the vertex position being within $|z| < 60$ cm is determined to be $\epsilon_{z\mathrm{vtx}} = 92 \pm 2\%$.

Jet reconstruction efficiency. The results presented are based on events with at least two jets of $E_T^{\mathrm{jet}} > 10$ GeV. The reconstruction of such relatively low E_T jets in the CDF II calorimeters is prone to inefficiencies associated with the calorimeter measurement of particle energies and the jet reconstruction algorithm used. Jet reconstruction efficiencies are studied using Monte Carlo dijet event samples generated with PYTHIA 6.216 [21] and processed through a GEANT-based detector simulation [22]. Simulated jets are reconstructed at both particle and calorimeter levels using the same jet reconstruction algorithm as that used in the data analysis. Then, events with matched pairs

of particle and calorimeter level jets in y-ϕ space are selected satisfying the requirement of $\Delta R = [(y_{\mathrm{CAL}} - y_{\mathrm{HAD}})^2 + (\phi_{\mathrm{CAL}} - \phi_{\mathrm{HAD}})^2]^{1/2} \le 0.7$, where y_{CAL} (y_{HAD}) and ϕ_{CAL} (ϕ_{HAD}) are the rapidity and azimuthal angle of a calorimeter (particle) level jet. If more than one calorimeter level jet matches a hadron-level jet, the closest matched calorimeter level jet is chosen. Using this method, the jet reconstruction efficiency ϵ_{jet}, defined as the fraction of hadron-level jets that have a matched calorimeter level jet, is obtained as a function of hadron-level jet E_T and η. We find that the value of ϵ_{jet} is $\sim 83\%$ at $E_T^{\mathrm{jet}} = 10$ GeV and reaches full efficiency at $E_T^{\mathrm{jet}} \sim 25$ GeV. The dijet reconstruction efficiency for a given DPE event, $\epsilon_{\mathrm{dijet}}$, is determined from the jet reconstruction efficiencies for the E_T and η of the jets in the event. In evaluating cross sections, each DPE dijet event is assigned a weight of $\epsilon_{\mathrm{dijet}}^{-1}$, and the number of DPE dijet events is recalculated.

D. Jet E_T energy smearing

The reconstruction of low E_T jets suffers from energy smearing effects due to large fluctuations in the calorimeter response to low E_T particles. These effects, convoluted with a steeply falling E_T^{jet} spectrum, cause migration of jets into adjacent E_T^{jet} bins. The smearing is unfolded as a function of E_T^{jet} using correction factors derived from inclusive DPE dijet events generated with the POMWIG Monte Carlo simulation [23], described in Sec. VI A, followed by a simulation of the detector. The E_T^{jet} spectra of the second highest E_T jet at particle and calorimeter levels are then compared. No matching between particle and calorimeter level jets in y-ϕ space is performed. The second highest E_T^{jet} is used in order to conform with the minimum E_T^{jet} thresholds imposed on E_T^{jet2} in our cross section measurements and in available theoretical predictions. Calorimeter level jets are corrected for the relative response of the calorimeters and for the absolute energy scale. The correction factors, obtained for each E_T^{jet2} bin as the ratio of the number of particle level jets to the number of calorimeter level jets, vary from 0.93 ± 0.03 to 1.03 ± 0.03 within the region of $10 < E_T^{\mathrm{jet2}} < 50$ GeV. This correction is applied to the measured inclusive DPE dijet cross section as a function of E_T^{jet2}.

VI. EXCLUSIVE DIJET PRODUCTION

The exclusive dijet signal contained in the IDPE data sample is evaluated from the distribution of the dijet mass fraction, R_{jj} ($= M_{jj}/M_X$), by measuring the excess of events at high R_{jj} over expectations from the POMWIG Monte Carlo DPE event generator [23], which does not simulate the exclusive process. Below, in Sec. VI A, we

demonstrate that the IDPE dijet data are well described by a combination of an inclusive MC generated distribution plus a non-DPE background obtained from data, in Sec. VI B we present the search for an exclusive dijet signal at high R_{jj}, in Sec. VI C we discuss expectations from an exclusive dijet Monte Carlo simulation, and in Sec. VI D we compare the data with an appropriately normalized combination of inclusive plus exclusive MC generated events. Cross section results for exclusive dijet production are presented in Sec. VII.

A. Inclusive POMWIG Monte Carlo Simulation

We first compare data distribution shapes with POMWIG predictions to verify that the data are well described by the MC simulation apart from deviations expected from the possible presence in the data of an exclusive dijet signal. The data used are the IDPE event sample defined in Eq. (7) in Sec. IV, which contains 20 414 events. While this sample should contain a larger fraction of exclusive dijet events than the total DPE event sample defined in Eq. (5), it is used because in searching for an exclusive signal, agreement between POMWIG predictions and data is more relevant if checked in a kinematic region as close as possible to that where the exclusive signal is expected.

Dijet events are generated in POMWIG using a $2 \rightarrow 2$ process with Pomeron remnants [see Eq. (3)] and a minimum transverse momentum cut of $p_T^{\mathrm{min}} = 7$ GeV/c. Each event is processed through the detector simulation and is required to pass the data analysis cuts. In comparisons with IDPE data, the SD and ND backgrounds expected in the data are normalized to their respective 14.0% and 13.3% values, estimated as described above in Sec. V, and are added to the POMWIG generated events. The MC distributions of POMWIG DPE plus SD and ND background events and the corresponding data distributions are normalized to the same area. Background SD distribution shapes are obtained from data satisfying the IDPE event sample requirements except for $\overline{\mathrm{BSC}_p}$, which is replaced by $\mathrm{N}_{\mathrm{BSC1}}^p + \mathrm{N}_{\mathrm{MP}}^p \le 1$ and $\mathrm{N}_{\mathrm{CLC}}^p \le 1$ excluding events with $\mathrm{N}_{\mathrm{BSC1}}^p = \mathrm{N}_{\mathrm{MP}}^p = \mathrm{N}_{\mathrm{CLC}}^p = 0$; ND shapes are extracted from J5 data satisfying the LRG_p and $\xi_{\bar{p}}^X$ requirements.

As a diffractive/Pomeron structure function we use $F_{jj}^D(\beta, Q^2) \propto \beta^{-1}$ [24], where β is the longitudinal momentum fraction of the parton in the Pomeron related to the x-Bjorken variable x_{Bj} (x-value of the struck parton) by $\beta \equiv x_{Bj}/\xi$. The Q^2 dependence of F_{jj}^D is implemented as a weight to $F_{jj}^D(\beta)$, determined from the CTEQ6L [25] proton parton distribution function (PDF) at the Q^2 scale of the event. The justification for using the proton PDF is based on a Run II CDF measurement of a rather flat Q^2 dependence of the ratio of SD to ND structure functions, indicating that the Pomeron evolves with Q^2 similarly to the proton [26]. We assign 46% and 54% of the Pomeron momentum to quarks (u, d, $\bar{u}$, $\bar{d}$) and gluons, respectively,

as measured by CDF in Run I from diffractive *W*, dijet, and *b*-quark production [27]. In view of the above considerations, the following structure function form is employed in the MC program:

$$F_{jj}^D(\beta, Q^2) = 0.46 \cdot \frac{1}{4} \sum_{q=u,d,\bar{u},\bar{d}} \left[\frac{\omega_q(Q^2)}{\beta_q + a} \right] + 0.54 \cdot \frac{\omega_g(Q^2)}{\beta_g + a},$$

(10)

where $\omega_{q(g)}(Q^2)$ is a weight used to include the Q^2 dependence of the quark (gluon) PDF and $a = 10^{-5}$ is an arbitrary parameter employed to avoid a divergence at $\beta = 0$.

Diffractive/Pomeron structure functions (DSFs) are also provided in the POMWIG MC program, obtained from QCD analyses of H1 diffractive DIS data [28]. Two of the H1 DSFs used in POMWIG are the H1 LO QCD fit2 (H1-fit2) with a Q^2 range extended to 10^5 GeV^2 to cover the CDF range [29], and the H1 NLO QCD fit3 (H1-fit3). Recently, QCD analyses of diffractive structure functions have also been performed by the ZEUS collaboration using diffractive DIS data obtained with a leading proton spectrometer (LPS) [30], and also by the rapidity gap (or Mx) method [31]. We have implemented programs returning NLO QCD fits for ZEUS-LPS and ZEUS-Mx structure functions for use in POMWIG (see Ref. [32] for Mx data). However, a more recent QCD analysis of diffractive DIS data performed by H1 using larger data samples and incorporating data from different final states [33] yields DSFs favoring the H1-fit2 DSF over the H1-fit3 DSF and in good shape agreement with the ZEUS-LPS DSF, while disfavoring the ZEUS-Mx DSF. Therefore, for consistency among measured DSFs at HERA, we exclude the H1-fit3 and ZEUS-Mx DSFs from this analysis.

Guided by our Run I DPE dijet analysis results, in which F_{jj}^D measured from the ratio of DPE to SD dijet events was found to agree in shape and normalization with H1-fit2, while the F_{jj}^D of Eq. (10) measured from diffractive dijet production is suppressed by a factor of ~ 10 relative to that from H1-fit2, we use F_{jj}^D of Eq. (10) for the Pomeron emitted by the $p(\bar{p})$ and H1-fit2 for that emitted by the $\bar{p}(p)$ [26]. This combination, which will be referred to as CDF $\oplus$ H1, is used as the default DSF in the POMWIG event generation. The four diffractive/Pomeron structure functions used in the analysis are listed in Table I.

In Fig. 8, we compare (a) the average dijet E_T^{jet} and (b) the average η^{jet} distributions, E_T^* and η^*, between IDPE data and POMWIG generated events using CDF $\oplus$ H1, CDF, H1-fit2, and ZEUS-LPS diffractive/Pomeron structure functions. While all E_T^* distributions have similar shapes, the data η^* distribution is broader than all simulated ones. The larger width of the data η^* distribution is due to the presence in the data of exclusive signal events concentrated in the pseudorapidity region around $\eta \sim -1$ (see Sec. VI D). Figure 9 shows data and POMWIG distributions of the dijet invariant mass, M_{jj}, and mass of the central hadronic system, M_X, where $M_X = [(\sum_{i=1}^{N_{tower}} E_i)^2 - (\sum_{i=1}^{N_{tower}} E_i \vec{n}_i)^2]^{1/2}$, where E_i is the energy of a tower with $E_T > 100$ MeV for CCAL or PCAL and $E_T > 20$ MeV for MPCAL and $\vec{n}_i$ is a unit vector pointing to the center of the tower. Good agreement is observed between data and MC generated distributions for all four diffractive/Pomeron structure functions.

B. Search for exclusive dijets

We search for exclusive dijet production by comparing data with POMWIG simulated dijet mass fraction distributions, $R_{jj} = M_{jj}/M_X$, looking for an excess of data over simulation at high R_{jj}. Data and four POMWIG R_{jj} distributions obtained with CDF $\oplus$ H1, CDF, H1-fit2, and ZEUS-LPS DSFs are shown in Fig. 10. All distributions are normalized to unit area.

An excess of data over simulated events at high R_{jj} is observed for all four DSFs used in the simulation. This excess is examined for consistency with the presence in the data of an exclusive dijet signal by applying selection cuts expected to enhance the appearance of the signal. The following successive cuts have been studied:

(a) LRG$_{\bar{p}}$: This cut, which is the equivalent of LRG$_p$, retains events with N$_{BSC1}^{\bar{p}}$ = N$_{MP}^{\bar{p}}$ = N$_{CLC}^{\bar{p}}$ = 0, enforcing a gap approximately covering the region $-5.9 < \eta < -3.6$.

(b) $E_T^{jet3} < 5$ GeV: third jet veto. Applying a veto on events with three (or more) jets of $E_T^{jet3} \geq 5$ GeV further enhances the exclusive dijet signal, resulting in a narrower exclusive signal peak in the R_{jj} distribution. This requirement tends to shift events toward high R_{jj} values by removing, for instance,

TABLE I. Diffractive/Pomeron structure function used in the inclusive dijet POMWIG Monte Carlo simulations.

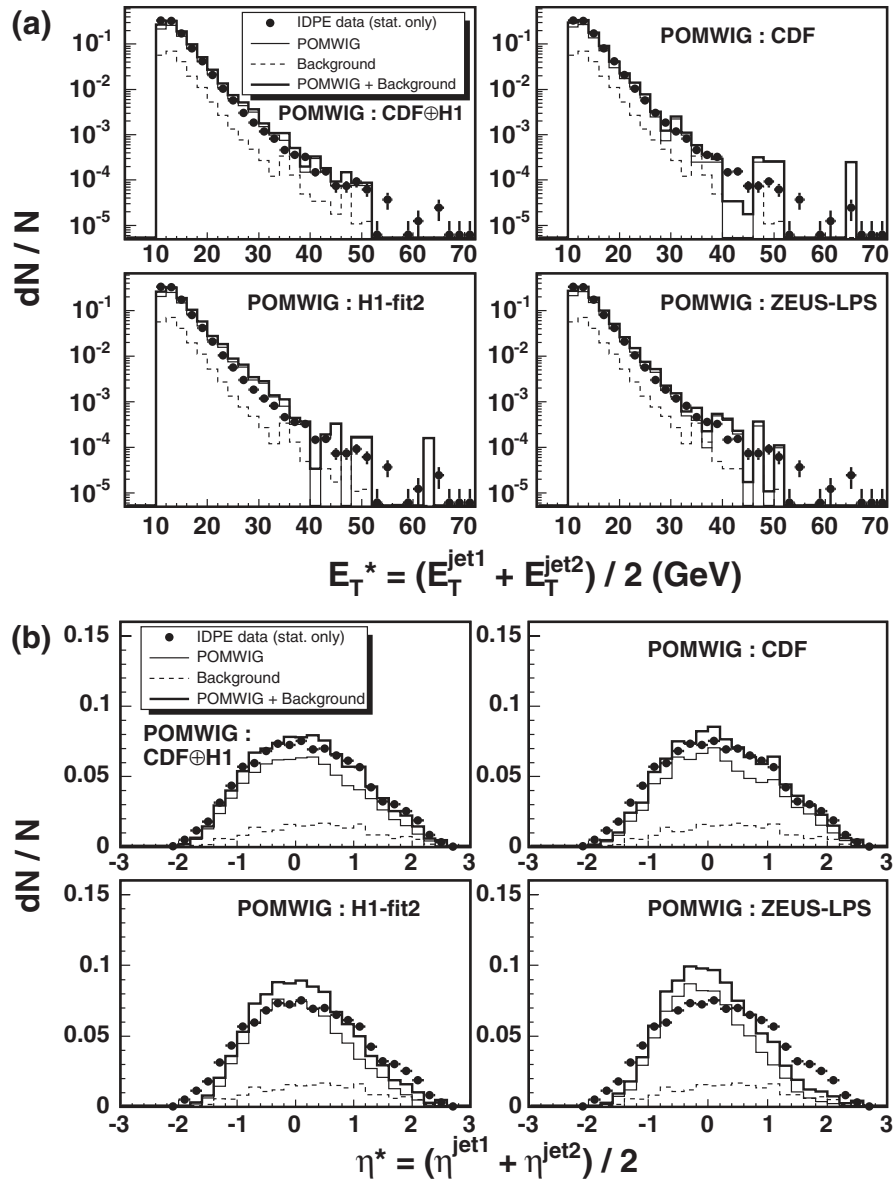| DSF	Definition
CDF $\oplus$ H1	$F_{jj}^D(\beta, Q^2)$ of Eq. (10) for $\mathbb{P}_{p(\bar{p})}$ and H1 LO QCD fit2 for $\mathbb{P}_{\bar{p}(p)}$ [2,24]
CDF	$F_{jj}^D(\beta, Q^2)$ of Eq. (10) for both $\mathbb{P}_p$ and $\mathbb{P}_{\bar{p}}$ [24]
H1-fit2	H1 LO QCD fit2 with extended Q^2 range [28]
ZEUS-LPS	NLO QCD fit to ZEUS-LPS data [30]

FIG. 8.   (a) Mean transverse energy E_T^* and (b) mean pseudorapidity η^* of the two highest E_T jets in IDPE data (points) and POMWIG MC events (thick solid histograms) composed of POMWIG DPE signal (thin solid histograms) and the sum of SD and ND background events (dashed histograms). The data and POMWIG + background distributions are normalized to unit area. The POMWIG generated distributions in the plots (a) and (b) correspond to the four different diffractive/Pomeron structure functions used: CDF ⊕ H1, CDF, H1-fit2, and ZEUS-LPS.

exclusive dijet events which contain extra recon-structed jets originating from gluon radiation in parton showers. In evaluating exclusive cross sec-tions, the loss of such events is accounted for by correcting the data for the exclusive signal accep-tance obtained from exclusive dijet MC simulations.

(c) η^{jet}-cut: η^{jet1} and/or $\eta^{jet2} < -0.5$. This cut exploits correlations in the η^{jet1} vs η^{jet2} distribution, which is more symmetric around $\eta^{jet1} = \eta^{jet2} = 0$ for inclu-sive than for exclusive events.

Figure 11 shows η^{jet1} vs η^{jet2} distributions for DPE data satisfying all the above selection cuts, POMWIG dijet events

generated with the CDF ⊕ H1 DSF, and exclusive dijet events generated with two different exclusive dijet MC simulations, EXHUME and EXCLDPE, which are described below in Sec. VI C. The POMWIG generated events, which do not contain an explicit exclusive contribution, and the data, which are dominated by nonexclusive events, are scattered symmetrically around $\eta^{jet1} = \eta^{jet2} = 0$, as the requirements of LRG$_p$ and LRG$_{\bar{p}}$ accept the same range of momentum loss fractions $\xi_{\bar{p}}$ and ξ_p. Since, however, the recoil proton is not detected, the RPST trigger introduces a bias in the exclusive production case, resulting in an asym-metric $\mathbb{P}_{\bar{p}}$-$\mathbb{P}_p$ collision with $\xi_{\bar{p}} > \xi_p$, boosting the dijet
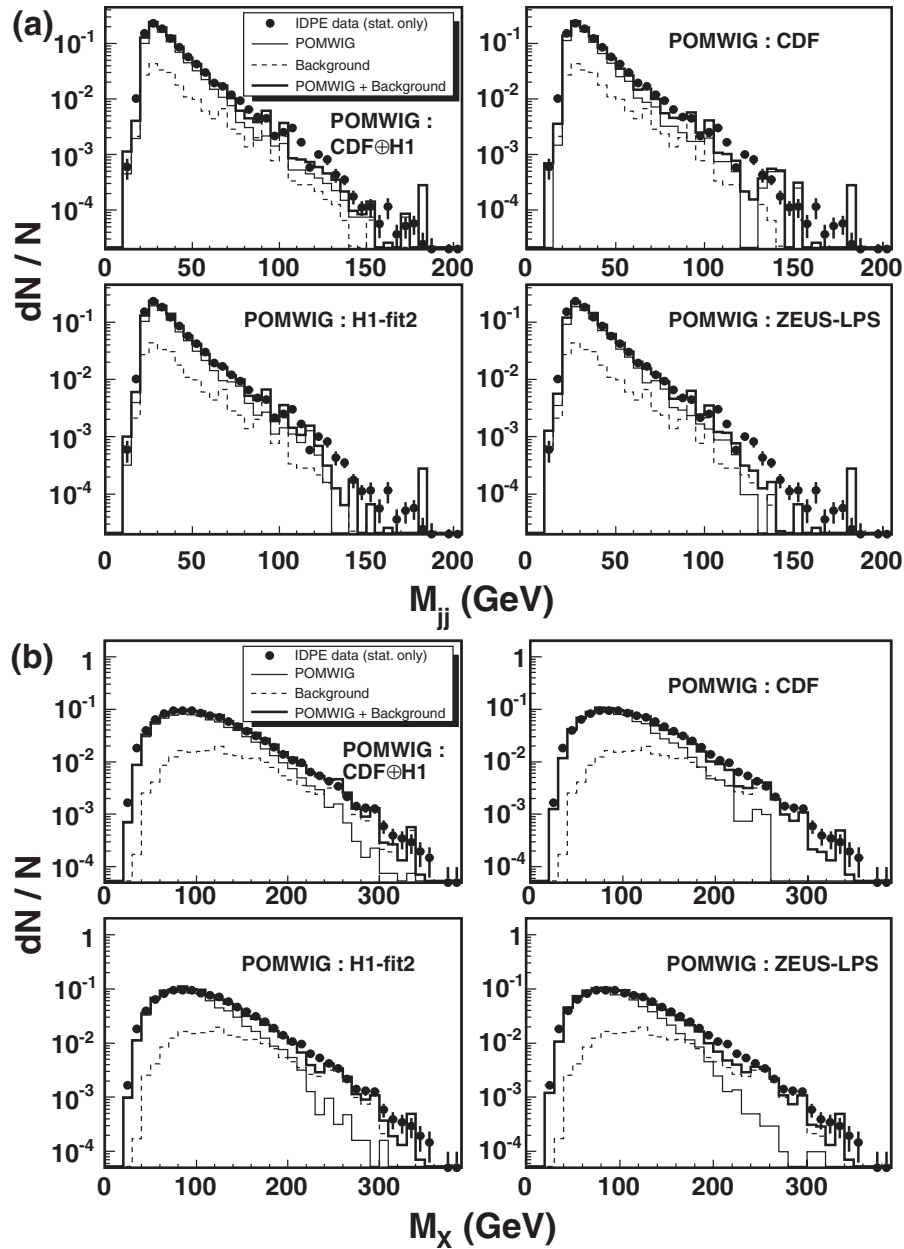
FIG. 9. (a) Dijet mass M_{jj} and (b) central hadronic system mass, M_X in IDPE data (points) and POMWIG MC events (thick solid histograms) composed of POMWIG generated DPE dijet events (thin solid histograms) and the sum of SD and ND generated background events (dashed histograms). The data and POMWIG + background distributions are normalized to unit area. The POMWIG DPE distributions in each set of four plots correspond to the four different diffractive/Pomeron structure functions used: CDF $\oplus$ H1, CDF, H1-fit2, and ZEUS-LPS.

system toward negative η. We exploit this kinematic effect by splitting the data and the events generated by each MC simulation into two samples, A and B, defined in η^{jet1}-η^{jet2} space as shown in Fig. 11. The data samples A, for which at least one of the two leading jets has $\eta^{\text{jet}} < -0.5$, contains most of the exclusive signal events, while sample B, comprising all other events, has a much reduced exclusive contribution. In Fig. 12, we compare IDPE data distributions of E_T^*, η^*, M_{jj}, and M_X for the background-rich

region B with the corresponding POMWIG distributions obtained using the CDF $\oplus$ H1 DSF. Reasonable agreement between data and simulation is observed.

C. Exclusive dijet Monte Carlo simulations

In the current analysis, we use two Monte Carlo event programs for generating exclusive dijet events: EXHUME 1.3.1 [34] and DPEMC 2.5 [35]. EXHUME is a LO matrix
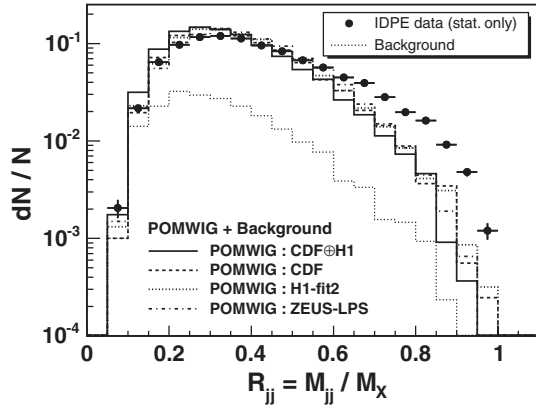
FIG. 10.   Dijet mass fraction, R_{jj}, in IDPE data (points) and POMWIG MC events (upper histograms), composed of POMWIG DPE signal and the sum of SD and ND background events (lower dashed histogram) normalized to the background fraction in the data. The upper four histograms correspond to the four different diffractive/Pomeron structure functions used in POMWIG: CDF ⊕ H1 (solid), CDF (dashed), H1-fit2 (dotted), and ZEUS-LPS (dot-dashed histogram). These four histograms and the data distribution are normalized to unit area.

element event generator founded on the perturbative calculations presented in Ref. [6], while exclusive dijet production in DPEMC 2.5 (EXCLDPE) is based on the DPE nonperturbative Regge theory inspired model of Ref. [5]. In EXHUME, we generate exclusive events using the MRST2002 next-to-leading order proton PDF [36], and implement parton showering and hadronization using PYTHIA. In EXCLDPE, we generate exclusive dijet events with the default parameters, using HERWIG 6.505 [37] to simulate parton showering and hadronization.

Distribution shapes of E_T^*, η^*, and R_{jj} for POMWIG DPE events and for events generated by EXHUME and EXCLDPE are compared in Fig. 13. All distributions are produced using quantities reconstructed at the hadron level for events selected with $E_T^{jet1,2} > 10$ GeV, $|\eta^{jet1,2}| < 2.5$, $0.03 < \xi_{\bar{p}} < 0.08$, and $3.6 < |\eta^{gap}| < 5.9$. The E_T^* spectrum is harder (much harder) in EXHUME (EXCLDPE) than in POMWIG, while the dijet system in both EXHUME and EXCLDPE is boosted toward negative η^* owing to the selected $\xi_{\bar{p}}$ range, as explained above in Sec. VI B. In the R_{jj} distributions, the exclusive jets emerge around
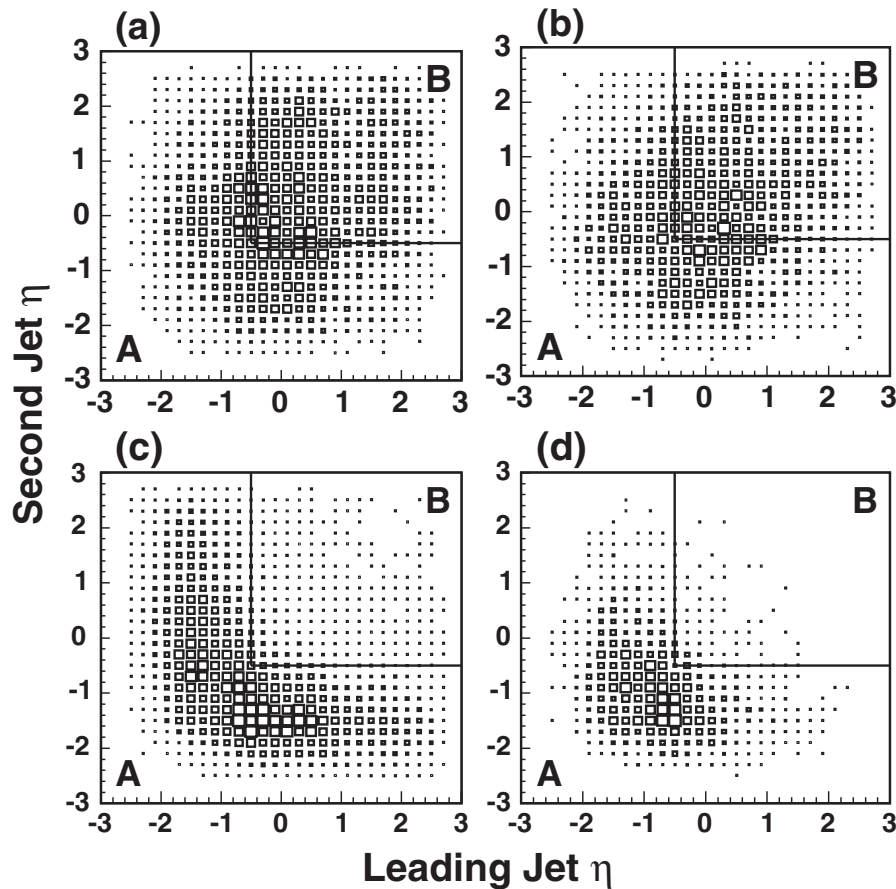
FIG. 11.   Second jet η vs leading jet η for events with two jets of $E_T^{jet1,jet2} > 10$ GeV satisfying all IDPE requirements plus the additional requirements of $LRG_{\bar{p}}$ and $E_T^{jet3} < 5$ GeV (third jet veto): (a) data, (b) POMWIG generated events, (c) exclusive EXCLDPE generated events, and (d) exclusive EXHUME generated events. The solid lines represent the η^{jet}-cuts of η^{jet1} and/or $\eta^{jet2} < -0.5$ used to divide the η^{jet1}-η^{jet2} space into the exclusive signal-enriched region A and the nonexclusive dominated region B.
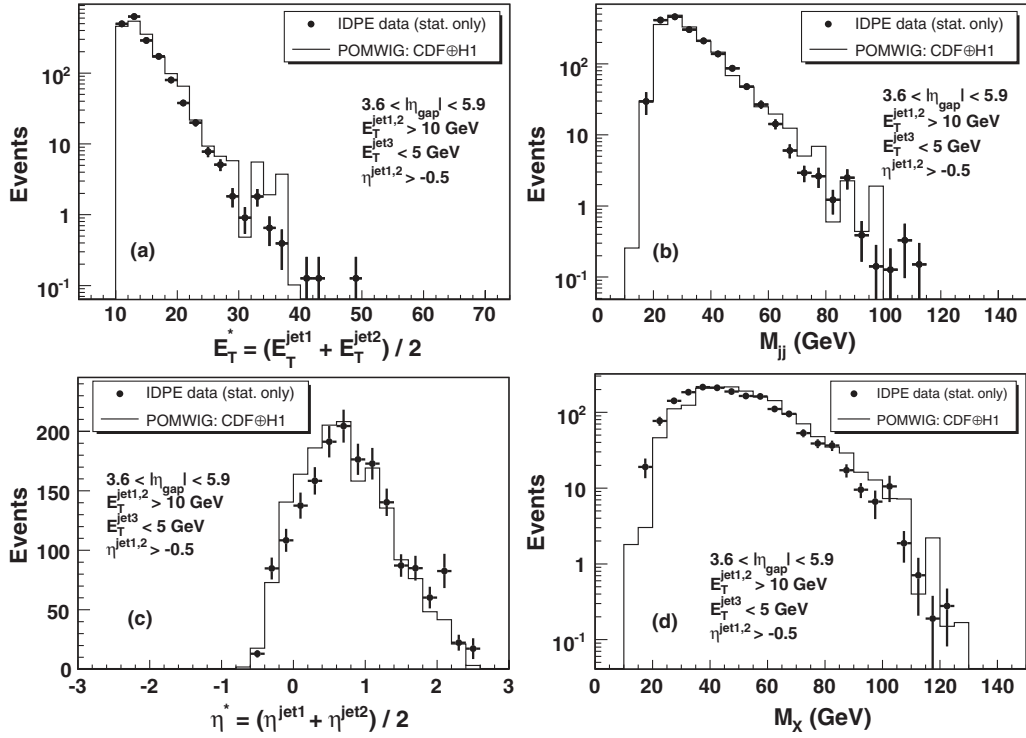
FIG. 12. Comparison of IDPE data distributions of (a) E_T^*, (b) M_{jj}, (c) η^*, and (d) M_X for the background-rich region B with corresponding POMWIG distributions obtained using the CDF ⊕ H1 DSF; the events plotted are those used in plots (a) and (b) of Fig. 11.
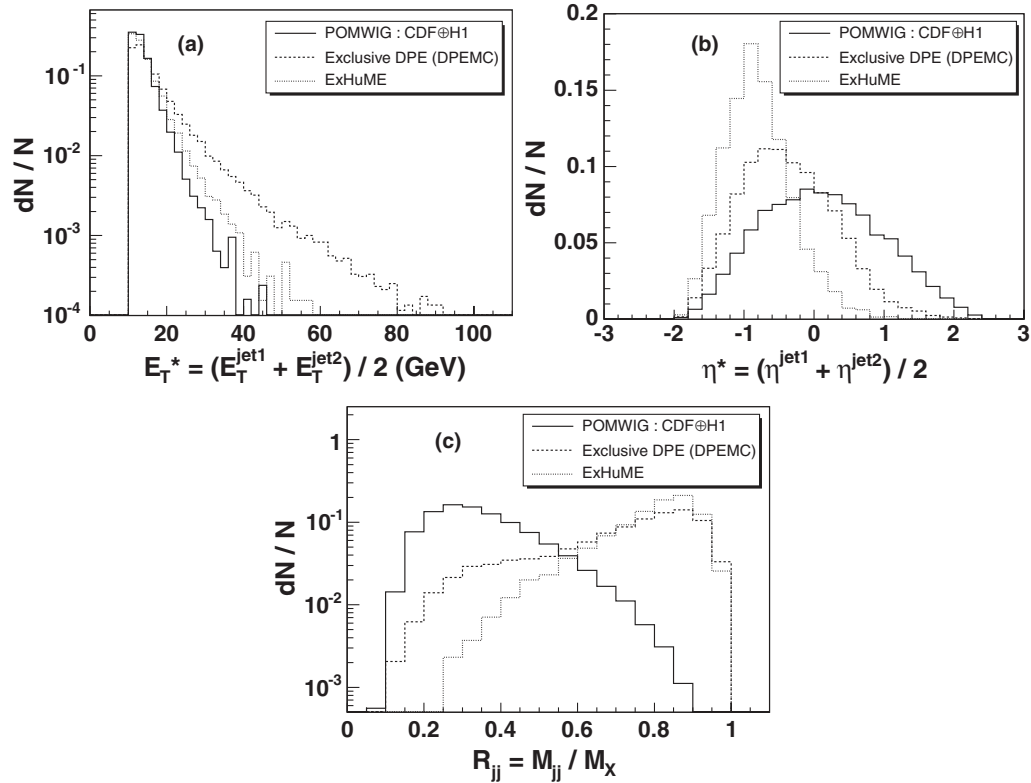

FIG. 13. (a) Mean E_T^{jet} of the two leading jets, E_T^*, (b) mean η^{jet}, η^*, and (c) dijet mass fraction, R_{jj} for POMWIG DPE dijet events generated using the CDF ⊕ H1 DSF diffractive/Pomeron structure function (solid histograms), and for exclusive dijet events generated with the EXCLDPE (dashed histograms) and EXHUME MC simulations (dotted histograms). All distributions are normalized to unit area.

$R_{jj} \sim 0.8$, while POMWIG events populate the low R_{jj} region. Both EXHUME and EXCLDPE MC distributions exhibit a long tail extending toward small R_{jj} values due to gluon radiation. For comparison with data, the MC generated events are processed through a detector simulation.

D. Comparison of data with combinations of inclusive and exclusive simulated events

We first fit the R_{jj} distribution of inclusive DPE dijet events satisfying the additional cuts (a) and (b) of Sec. VI B, but not requiring the η^{jet}-cut. Results are shown in Fig. 14. In plots (a) and (b) the two highest E_T jets in an event are required to have $E_T^{jet1,2} > 10$ GeV and in plots (c) and (d) >25 GeV. The solid histogram in each plot is obtained from a binned maximum likelihood fit of the data with a combination of (i) POMWIG DPE plus SD and ND background events (dashed histograms) and (ii) exclusive signal events (shaded histograms) generated by EXHUME for plots (a) and (c) or EXCLDPE for plots (b) and (d) satisfying the same cuts as the data. In each fit, the normalizations of the inclusive POMWIG and of the exclusive MC events are introduced as free parameters. The R_{jj} data distribution is well reproduced within statistical uncertainties with both EXHUME and EXCLDPE based exclusive contributions, yielding exclusive fractions of $F_{excl} = 15.0 \pm 1.2$(stat.)% and $F_{excl} = 15.8 \pm 1.3$(stat.)%, respectively, for $E_T^{jet1,2} > 10$ GeV.

As a control check, we add the requirement of the η^{jet}-cut and obtain distributions for data, POMWIG, EXHUME, and POMWIG + EXHUME events separately for samples B and A, shown in Figs. 15(a) and 15(b), respectively. The relative normalizations of the total DPE data and MC event samples are fixed to those obtained in the fits of Fig. 14(a), and the R_{jj} distributions are scaled by the number of events that pass the η^{jet}-cuts that define the data samples. As expected, no significant exclusive contribution is observed in the data sample B. In sample A, good agreement is observed between the data and the POMWIG + EXHUME combination, indicating that the observed excess at high R_{jj}, whose fraction in the data has increased from 15.0 ± 1.2(stat)% to 20.8 ± 0.8(stat)% by the sample A selection cuts, is consistent with an exclusive signal in both shape and relative normalization. Similar agreement is observed using the EXCLDPE simulation.

The fit of the data with MC simulated events would be expected to improve if the normalizations were left free to be determined by the fit. Binned maximum likelihood fits to the data of sample A are shown in Fig. 16. The fraction of exclusive dijet signal, F_{excl}, is found to be 23.0 ± 1.9(stat)% for EXCLDPE and 22.1 ± 1.8(stat)% for EXHUME.

In Fig. 17, we compare the η^* distribution of the data of sample A with a MC generated distribution using POMWIG with the CDF $\oplus$ H1 diffractive structure function and an
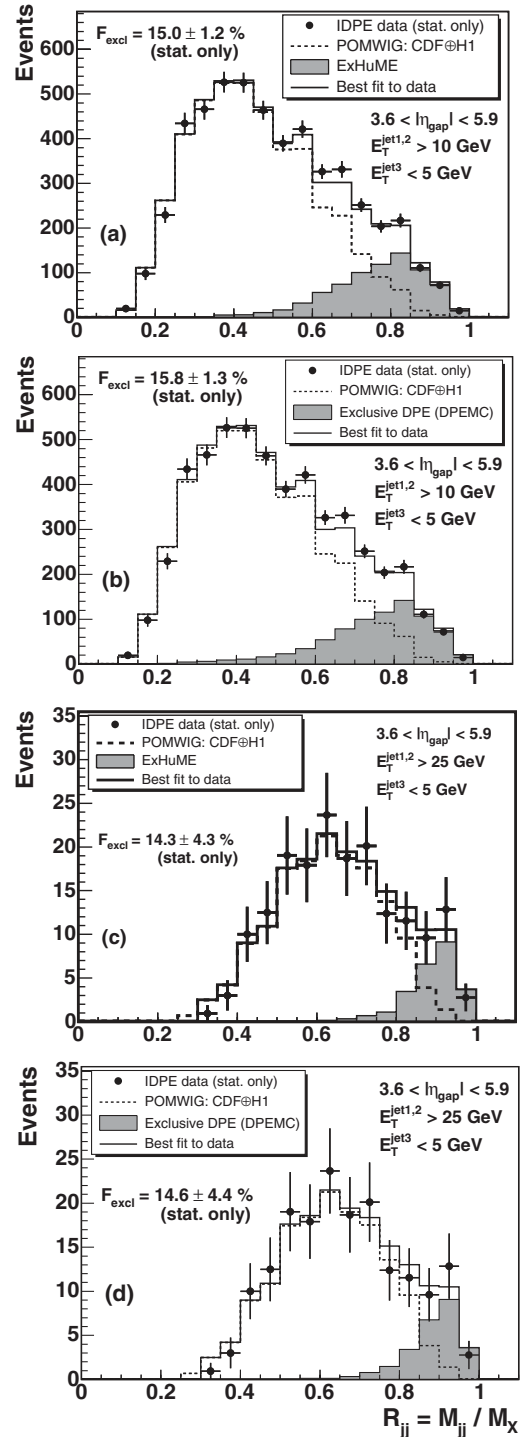

FIG. 14.   Dijet mass fraction in IDPE data (points) and best fit (solid histograms) with a mixture of (i) POMWIG generated events composed of POMWIG DPE signal and SD plus ND background events (dashed histogram), and (ii) exclusive dijet MC events (shaded histogram). The data and the MC events are selected from the respective IDPE samples after applying the additional veto cuts of $LRG_{\bar{p}}$ and $E_T^{jet3} < 5$ GeV. Plots (a) and (c) [(b) and (d)] present fits using EXHUME [EXCLDPE] generated exclusive dijet events, while a requirement of $E_T^{jet2} > 10$ GeV [25 GeV] is applied to plots (a) and (b) [(c) and (d)].
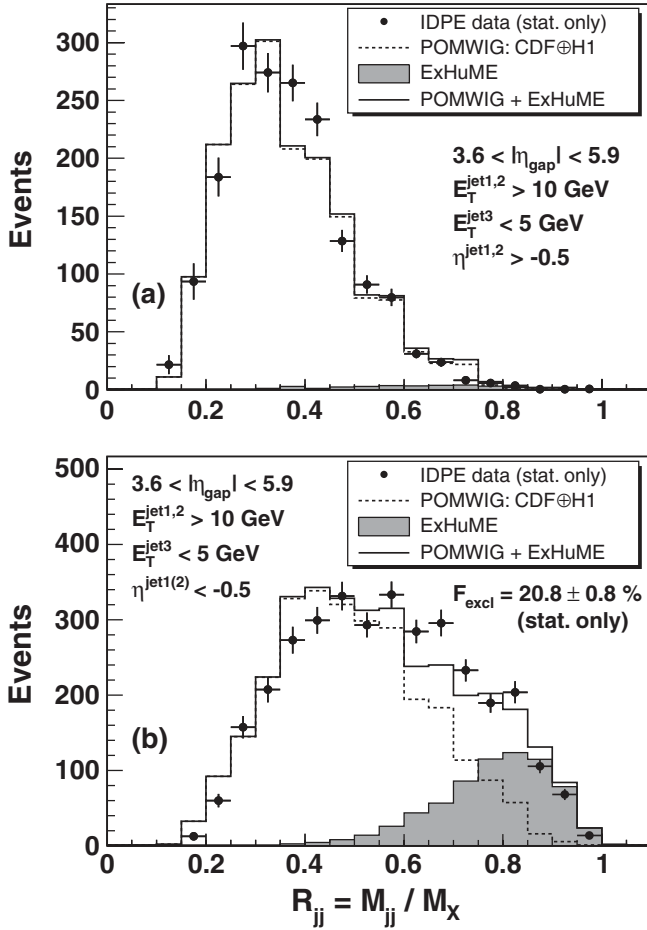
FIG. 15. Dijet mass fraction for IDPE data (points) and for POMWIG generated events (dashed histogram) composed of POMWIG DPE plus SD and ND background events, and for EXHUME generated exclusive dijet events (shaded histograms). The solid histogram is the sum of POMWIG ⊕ EXHUME events. Plot (a) shows distributions for event sample B, and plot (b) for event sample A. The events plotted pass all other selection cuts. The MC events are normalized using the results of the fits shown in Fig. 14(a), scaled according to the actual number of events that pass the η^{jet}-cut requirement.
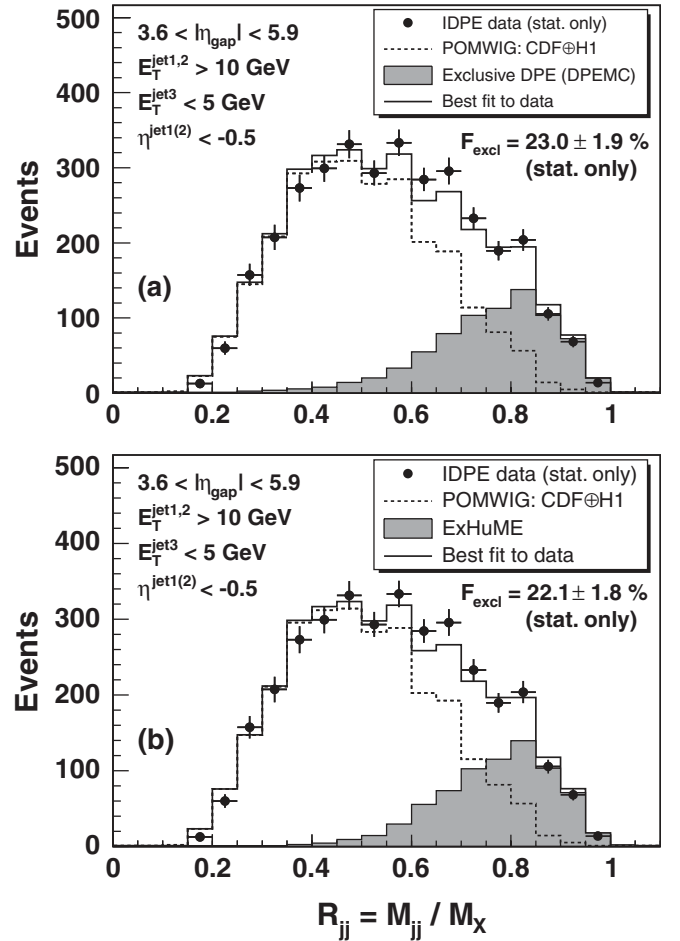
FIG. 16. Dijet mass fraction for IDPE data (points) and best fit (solid histogram) to the data obtained from a combination of POMWIG events (dashed histogram) composed of POMWIG DPE plus SD and ND background events, and exclusive dijet MC events (shaded histogram) generated using (a) EXCLDPE or (b) EXHUME. The data and the MC events are from sample A and are required to pass all other selection cuts.

admixture of an exclusive signal of (a) 23% EXCLDPE or (b) 22% EXHUME generated events, where the normalization was fixed to that obtained from the fits in Fig. 16. Considering that the normalization was not allowed to vary in performing the fit, reasonable agreement between data and simulation is observed, confirming our previous assertion that the broader data than POMWIG simulated distribution seen in Fig. 8 is due to the exclusive contribution in the region around $\eta^* \sim -1$.

To determine the sensitivity to the DSFs used in the simulations, we have extracted the fraction F_{excl} using eight different combinations of DSFs, made up from each of the four DSFs used in POMWIG (CDF ⊕ H1, CDF, H1-fit2 and ZEUS-LPS) with the DSF used in EXHUME or in EXCLDPE. The eight F_{excl} values obtained, listed in Table II,

are mutually consistent within the quoted statistical uncertainties.

VII. RESULTS

In this section we present results for both inclusive DPE dijet cross sections, $\sigma_{\text{DPE}}^{\text{incl}}$, and for exclusive production, $\sigma_{jj}^{\text{excl}}$. The inclusive cross sections are evaluated from the IDPE dijet data sample defined by the selection cuts listed in Eq. (7). Although the exclusive events are expected to be concentrated in the region of $0.03 < \xi_{\bar{p}} < 0.08$, as determined from simulations and from a subsample of the data with recorded RPS tracking information, the larger $\xi_{\bar{p}}^X$ range of $0.01 < \xi_{\bar{p}}^X < 0.12$ is used to ensure that there are no inefficiencies caused by resolution and/or possible systematic effects associated with the calorimeter based definition of $\xi_{\bar{p}}$ [26]. The results are corrected for backgrounds falling within this larger $\xi_{\bar{p}}^X$ region.
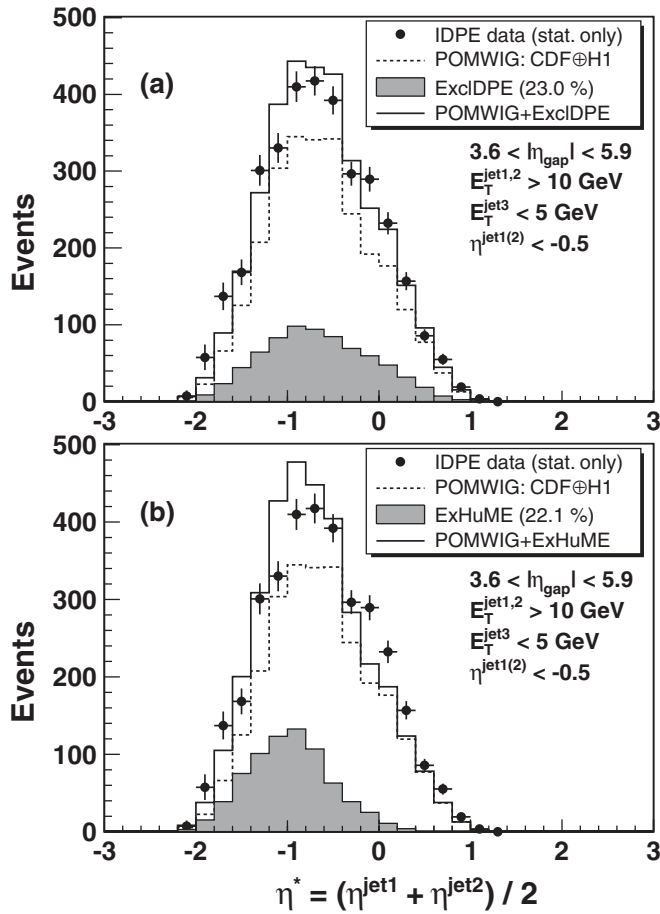
FIG. 17. Comparison of mean pseudorapidity distributions η^* between the IDPE data of sample A and the mixture of POMWIG and (a) EXCLDPE or (b) EXHUME simulated events normalized by the fit presented in Fig. 16.

Exclusive cross sections are obtained by scaling $\sigma_{\mathrm{DPE}}^{\mathrm{incl}}$ by the fraction of IDPE data that pass veto cuts (a), (b), and (c) of Sec. VI B and multiplying the result by $F_{\mathrm{excl}} \cdot A_{\mathrm{excl}}^{-1}$, where F_{excl} is the exclusive fraction and A_{excl} the acceptance of the veto cut(s) for exclusive events. As the veto

TABLE II. Fraction of exclusive dijet events in DPE dijet data, extracted from likelihood fits to data selected with the requirements of $E_T^{\mathrm{jet1,2}} > 10$ GeV, $E_T^{\mathrm{jet3}} < 5$ GeV, $\eta^{\mathrm{jet1,2}} > -2.5$, $\eta^{\mathrm{jet1(2)}} < -0.5$, $0.03 < \xi_{\bar{p}} < 0.08$ and $3.6 < |\eta^{\mathrm{gap}}| < 5.9$, using combinations of POMWIG + EXHUME or POMWIG + EXCLDPE distribution shapes. Results are listed for four different DSFs used in POMWIG. The $\eta^{\mathrm{jet1(2)}} < -0.5$ cut requires that at least one of the two highest E_T jets be within $\eta_{\mathrm{jet}} < -0.5$. Uncertainties are statistical only.

DSF	EXCLDPE	EXHUME
CDF $\oplus$ H1	$23.0 \pm 1.9\%$	$22.1 \pm 1.8\%$
CDF	$22.6 \pm 1.9\%$	$21.7 \pm 1.8\%$
H1-fit2	$26.0 \pm 2.1\%$	$24.7 \pm 2.0\%$
ZEUS-LPS	$25.4 \pm 2.1\%$	$24.3 \pm 2.0\%$

cuts include a $LRG_{\bar{p}}$ requirement, we recalculate the correction for spoiled gaps due to multiple $\bar{p}p$ interactions with no vertices. We then scale $\sigma_{\mathrm{DPE}}^{\mathrm{incl}}$ by the ratio of the correction for $p \oplus \bar{p}$ gaps to that for only a p-gap and apply it in evaluating $\sigma_{jj}^{\mathrm{excl}}$. The acceptance of the exclusive cuts, A_{excl}, is obtained from the fraction of EXHUME or EXCLDPE generated events passing the same cuts.

In the following sections, we summarize the methods we used to calculate systematic uncertainties and their contributions to the total uncertainty.

A. Jet E_T smearing

The large difference in the slope of the E_T^{jet} distributions between inclusive POMWIG and exclusive MC generated events seen in Fig. 13 results in different corrections for E_T^{jet} smearing. Corrections for EXHUME and EXCLDPE generated events are derived using the method described in Sec. V D. In obtaining the final results for $\sigma_{jj}^{\mathrm{excl}}$ using EXHUME, the cross sections extracted by the above procedure are multiplied by the ratio of the corrections obtained from the EXHUME event sample to the POMWIG based corrections to account for the difference in E_T^{jet} spectra.

B. Systematic uncertainties

The systematic uncertainty in the exclusive fraction receives contributions from uncertainties in the jet energy scale, unclustered calorimeter energy determination, jet trigger efficiency, jet E_T smearing, non-DPE background, RPS acceptance, luminosity determination, knowledge of the diffractive structure function, statistics of MC event samples, underlying event determination, and the modeling of the underlying event.

1. Jet energy scale

The uncertainty in E_T^{jet} associated with the jet energy scale is evaluated by varying the uncertainties on the relative and absolute energy scale corrections by $\pm 1\sigma$ in estimating the efficiency for triggering on a single calorimeter tower of $E_T > 5$ GeV, while simultaneously monitoring the number of jets with E_T^{jet} above the desired threshold. Because of the steeply falling E_T^{jet} spectrum, the change in trigger efficiency increases with decreasing E_T^{jet} from $^{-26}_{+34}\%$ for $10 < E_T^{\mathrm{jet}} < 15$ GeV to $^{-11}_{+11}\%$ for $25 < E_T^{\mathrm{jet}} < 35$ GeV, resulting in a variation of the number of IDPE dijet events accepted of $\pm 21\%$ ($^{+32}_{-27}\%$) for $E_T^{\mathrm{jet2}} > 10$ GeV ($E_T^{\mathrm{jet2}} > 25$ GeV). This is the dominant uncertainty in both the inclusive and exclusive dijet cross section measurements.

2. Unclustered calorimeter energy

Uncertainties on the unclustered calorimeter energy scale affect the $\xi_{\bar{p}}^X$ measurement, which in turn leads to

uncertainties not only on the number of observed events, but also potentially on R_{jj} distribution shapes. However, the CCAL and PCAL energy scale uncertainties tend to cancel out in the R_{jj} ratio.

Changing the energy scale of CCAL and PCAL by $\pm 5\%$ in calculating $\xi_{\bar{p}}^{X}$ leads to a variation of $\pm 1\%$ in the inclusive DPE dijet cross sections for $E_T^{\text{jet1,2}} > 10$ GeV. Varying the MPCAL energy scale by $\pm 30\%$, independently of CCAL and PCAL, results in a cross section change of $^{-7}_{+10}\%$. This is due to more (less) events falling into the range of $0.01 < \xi_{\bar{p}}^{X} < 0.12$ when the MPCAL energy scale is lowered (raised). The number of data events at high R_{jj} is less affected by these changes, since the MPCAL is less active for such events. After adjusting the jet energy scale, the fraction of exclusive dijet signal in the DPE data is reevaluated by repeating the MC to data fits. The full difference between the number of inclusive events (exclusive signal fraction) obtained from the varied samples and that obtained from the default sample is assigned as a systematic uncertainty on this correction. The uncertainties on the exclusive cross sections propagated from these differences are $\pm 13\%$ ($\pm 21\%$) for $E_T^{\text{jet1,2}} > 10(25)$ GeV.

3. Jet trigger efficiency

Jet trigger efficiencies have been discussed in Sec. V C. The full difference of the efficiencies obtained from minimum-bias data and inclusive RPS triggered data is taken as a systematic uncertainty and propagated to an uncertainty on the exclusive signal fraction.

4. Jet E_T smearing

Corrections for inclusive DPE dijets are obtained from samples of POMWIG MC dijet events. Statistical uncertainties on the correction factors are taken as systematic uncertainties and propagated to uncertainties on $\sigma_{\text{DPE}}^{\text{incl}}$. The full difference between the exclusive dijet cross sections obtained using corrections derived from EXHUME and EXCLDPE MC generated events is assigned as a systematic uncertainty on the exclusive cross sections. This uncertainty is $\pm 4\%$ ($\pm 6\%$) for $E_T^{\text{jet1,2}} > 10(25)$ GeV.

5. Non-DPE background

The dominant non-DPE background uncertainty is associated with the SD background fraction of $F_{\text{BG}}^{SD} = 14 \pm 3\%$, which contributes an uncertainty on the cross sections of $\pm 0.03/(1 - 0.14) = \pm 3.5\%$. The $\pm 3\%$ uncertainty on F_{BG}^{SD} has a negligible effect on the R_{jj} shapes relative to other uncertainties.

6. RPS acceptance

The acceptance of the RPS trigger counters, A_{RPS}, could vary with beam conditions and changing counter efficien-

cies. During the data taking period, A_{RPS} varied by at most $\pm 6\%$. This value is assigned as a systematic uncertainty on A_{RPS} and propagated to both inclusive and exclusive cross sections.

7. Luminosity

The luminosity uncertainty, which is applied to all cross sections, is 5.9%, with 4.4% due to the acceptance and operation of the luminosity monitor and 4.0% due to the uncertainty in normalization using the total $\bar{p}p$ cross section [38].

8. Diffractive structure function

We have examined the effect of the choice of DSF on comparisons between data and POMWIG generated event distributions. We find that the H1-fit2 and ZEUS-LPS DSFs yield similar kinematic distribution shapes, which are in reasonable agreement with the data, while the H1-fit3 and ZEUS-M_X ones produce significantly different distributions and are clearly disfavored. Guided by these results, we use POMWIG events generated with the H1-fit2 DSF to perform the fits to the data and evaluate F_{excl} and take the full difference between the exclusive cross sections obtained and those extracted using the default DSF of CDF $\oplus$ H1 as a systematic uncertainty.

9. Statistics of Monte Carlo event samples

Statistical uncertainties in the MC generated events are taken into account in MC to data likelihood fits performed to extract F_{excl}, so that the uncertainty in F_{excl} is due to the uncertainties in both data and MC event samples. The MC
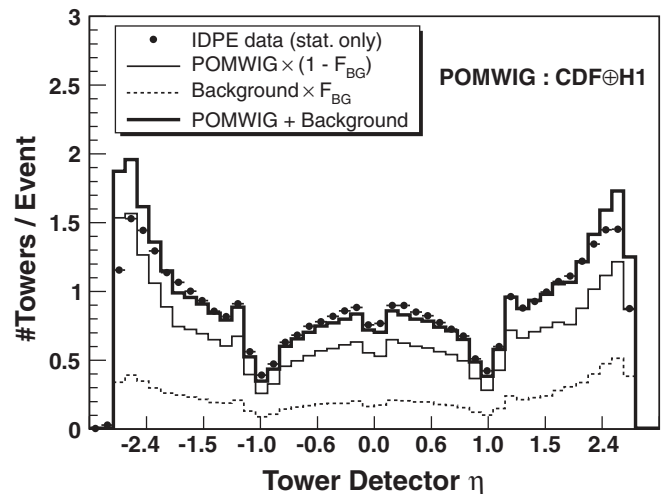

FIG. 18. The number of calorimeter towers per event with $E_T > 100$ MeV which are outside the jet cones versus tower detector η for IDPE data (points) and POMWIG MC events (thick line) composed of POMWIG DPE signal (thin line) and the sum of SD and ND background events (dashed line) normalized to the background fraction per event.

associated uncertainty is derived from the uncertainty in F_{excl} by quadratically subtracting the data uncertainty, determined from the number of events in the extracted signal, and propagated to the MC contribution to the exclusive cross section uncertainty.

10. Underlying event

The observed excess of data over simulated events at high R_{jj} in Fig. 16 could be due to an overestimate of the underlying event (UE) activity in the simulation. We investigated this possibility by following the methodology previously developed by CDF in generic UE studies in $p\bar{p}$ collisions [39]. The η-ϕ space is split into three regions with respect to the leading jet axis, the "forward" ($|\Delta\phi| < 60°$), the "transverse" ($60° < \Delta\phi < 120°$ or $240° <$

$\Delta\phi < 300°$), and the "away" region ($120° < \Delta\phi < 240°$), and the UE is evaluated in the transverse region, which is sensitive to the particles outside the jets.

Figure 18 shows the number of calorimeter towers outside the jet cones per event vs tower detector η for IDPE data and the simulation. Good agreement is observed, except for a discrepancy at the highest $|\eta|$ region, where the tower transverse size is smaller than that of hadron showers produced by particles interacting in the calorimeter. This results in several tower "hits" per particle at high $|\eta|$, which is difficult to accurately simulate.

A more relevant UE comparison between data and simulation is that of transverse calorimeter tower multiplicity (N_T) and E_T distributions between data and MC generated events, as shown in Fig. 19 for different R_{jj} bins in the range $0.5 < R_{jj} < 1.0$. Agreement between data and
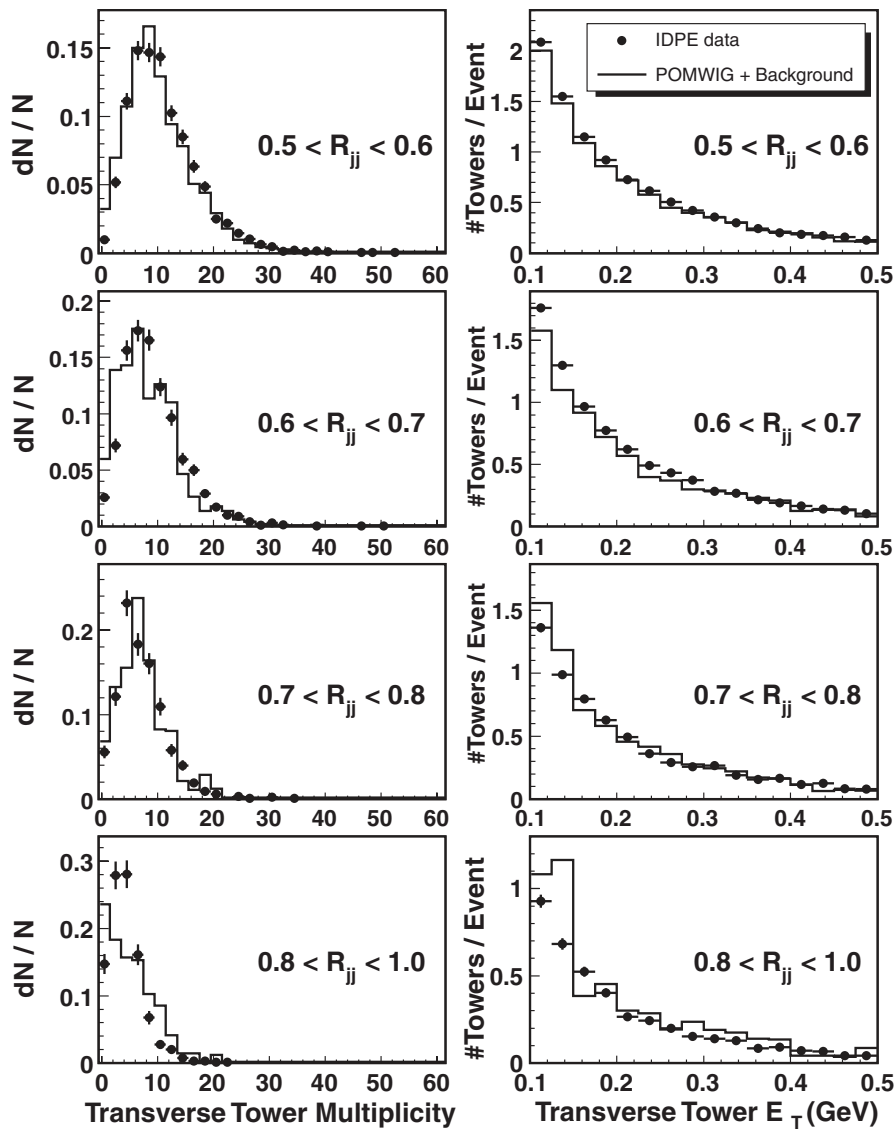

FIG. 19.   Calorimeter tower multiplicity and tower E_T distributions in the transverse region with respect to the leading jet axis ($60° < \Delta\phi < 120°$ or $240° < \Delta\phi < 300°$) for four R_{jj} bins in the region of $0.5 < R_{jj} < 0.9$. The tower multiplicity and tower E_T distributions are normalized to unit area and to the number of transverse towers per event, respectively.

TABLE III. Measured inclusive DPE and exclusive dijet cross sections, and the ratio of the exclusive to inclusive DPE dijet cross sections in the kinematic range $E_T^{jet1,2} > E_T^{min}$, $|\eta^{jet1,2}| < 2.5$, $0.03 < \xi_{\bar{p}} < 0.08$ (integrated over all $t_{\bar{p}}$), and $3.6 < \eta_{gap} < 5.9$.

E_T^{min}	$\sigma_{DPE}^{incl} \pm$ stat $\pm$ syst	$\sigma_{jj}^{excl} \pm$ stat $\pm$ syst	R_{incl}^{excl}
10 GeV	$14.5 \pm 0.1^{+9.8}_{-6.9}$ nb	$1.10 \pm 0.04^{+1.29}_{-0.54}$ nb	$7.6 \pm 0.3^{+2.9}_{-1.2}\%$
15 GeV	$1.43 \pm 0.02^{+0.89}_{-0.62}$ nb	$112 \pm 7^{+84}_{-49}$ pb	$7.8 \pm 0.5^{+3.2}_{-1.2}\%$
20 GeV	$267 \pm 6^{+166}_{-110}$ pb	$15.7 \pm 2.0^{+15.5}_{-9.6}$ pb	$5.9 \pm 0.8^{+3.0}_{-2.1}\%$
25 GeV	$76.0 \pm 2.7^{+37.0}_{-28.6}$ pb	$4.84 \pm 0.96^{+4.11}_{-3.28}$ pb	$6.4 \pm 1.3^{+4.6}_{-3.9}\%$
35 GeV	$14.6 \pm 1.2^{+5.3}_{-5.2}$ pb	$1.37 \pm 0.49^{+1.08}_{-1.01}$ pb	$9.3 \pm 3.4^{+6.9}_{-6.6}\%$

simulation is observed, except in the low multiplicity and low E_T regions where the data points fall below the MC generated histograms. To quantify the effect of this discrepancy on the extracted exclusive signal fraction, we compare transverse tower E_T distributions between data and MC in the region of $0.4 < R_{jj} < 0.7$, which is in the plateau of the distribution shown in Fig. 16 (to avoid edge effects). Then, we modify the UE in the simulation to minimize the χ^2/d.o.f. and reevaluate the exclusive fraction. Using the default MC simulation yields a χ^2/d.o.f = 1.4. The UE is modified by scaling the tower E_T of transverse calorimeter towers by a factor $F(E_T) = E_T \times (1.5 - N_T/40)$ for $N_T < 20$, yielding a χ^2/d.o.f. = 0.4, which is lower by 1 unit. The E_T scaling has the effect of fewer calorimeter towers being rejected by the calorimeter threshold cuts, thereby resulting in a larger exclusive signal fraction, $F_{excl}^{scaled} = 27.0 \pm 2.2$(stat)%. Since the discrepancy between the default and scaled MC distributions is only one unit of χ^2/d.o.f., we retain the default value for the fraction and use the scaled result to assign a systematic uncertainty of $\pm(F_{excl}^{scaled} - F_{excl}^{default})/F_{excl}^{default})/2 = \pm 9\%$.

11. Exclusive dijet model

The full difference between the exclusive cross section values obtained using the EXHUME and EXCLDPE MC R_{jj} shapes is assigned as a systematic uncertainty associated with the exclusive signal modeling (see Table III). This difference is mainly due to different amounts of radiation emitted from the jets.

C. Cross sections

Measured cross sections for inclusive DPE and exclusive dijet production, and the ratio of exclusive to inclusive DPE dijet cross sections for different $E_T^{jet1,2}$ thresholds, are presented in Table III. The listed systematic uncertainties consist of all those discussed above added in quadrature. The exclusive cross sections are plotted in Fig. 20(a), where they are compared with hadron-level predictions of EXHUME and EXCLDPE Monte Carlo simulations. The EXHUME predictions are favored by the data in both normalization and shape. The exclusive signal for $E_T^{jet1,2} > 10$ GeV is established at a significance level of
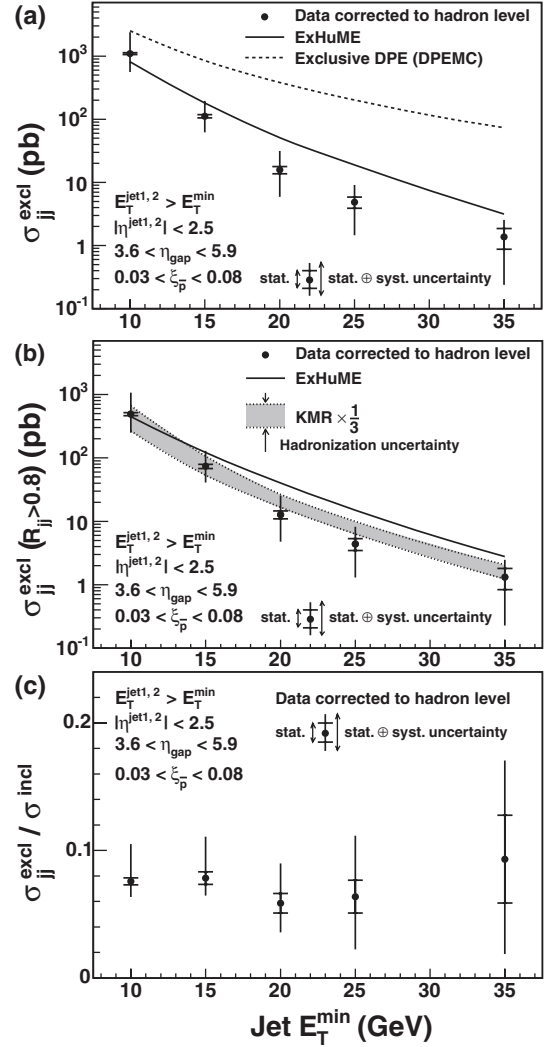

FIG. 20. Exclusive dijet cross sections for events with two jets of $E_T^{jet} > 10$ GeV plotted vs the minimum E_T^{jet} of the two jets in the kinematic range denoted in the figures: (a) total exclusive cross sections compared with EXHUME and EXCLDPE predictions; (b) exclusive cross sections for events with $R_{jj} > 0.8$ compared with EXHUME (solid curve) and with the LO analytical calculation from Ref. [6] (see also Ref. [42]) scaled down by a factor of 3 (dashed lines)—the shaded area represents uncertainties in the calculation due to hadronization effects; and (c) the ratio of total exclusive to inclusive DPE cross sections.

6.1σ, determined from the value of $R_{\mathrm{incl}}^{\mathrm{excl}} = 7.6 \pm 0.3_{-1.2}^{+2.9}\%$ presented in Table III. The value of 6.1σ is obtained as the ratio of the central value of $R_{\mathrm{incl}}^{\mathrm{excl}} = 7.6$ divided by an uncertainty composed of the statistical uncertainty of 0.3% and the "downward" systematic uncertainty of 1.2%, combined in quadrature and yielding $(0.3^2 + 1.2^2)^{1/2} = 1.24\%$, as the systematic uncertainty of -1.2% comes from an upward fluctuation of the background.

In Fig. 20(b), we compare the data exclusive cross section for events with $R_{jj} > 0.8$ plotted vs jet E_T^{min} with the EXHUME prediction and with the analytical calculation of exclusive dijet cross sections from Ref. [40] (KMR). The $\sigma_{jj}^{\mathrm{excl}}$ is recalculated using the observed exclusive signal in the region of $R_{jj} > 0.8$. The KMR cross sections, which are based on a LO parton level calculation of the process $gg \rightarrow gg$, have an $\mathcal{O}(3)$ systematic uncertainty. The kinematic cuts used in KMR are slightly different from those used in the present analysis, which could lead to an effect of $\sim \pm 20\%$ on the predicted cross section values [41]. The good agreement seen in Fig. 20 between the measured $\sigma_{jj}^{\mathrm{excl}}$ and the KMR predictions multiplied by a factor of $1/3$ suggests that the data are consistent with the KMR predictions within the quoted uncertainties. An even better agreement is reached by rescaling the parton transverse momentum in the KMR calculation to the measured jet transverse energy [42].

The ratio of exclusive to inclusive DPE dijet cross sections measured from the data as a function of jet E_T^{min} is shown in Fig. 20(c).

VIII. HEAVY FLAVOR QUARK JETS

One of the most characteristic features of exclusive dijet production is that at high dijet mass fraction it is dominated by the parton level process $gg \rightarrow gg$, as contributions from $gg \rightarrow q\bar{q}$ are suppressed. Born level cross sections for exclusive production of a color-singlet dijet system of mass M are given by [43]

$$\frac{d\hat{\sigma}_{\mathrm{excl}}}{dt}(gg \rightarrow gg) = \frac{9}{4} \frac{\pi \alpha_s^2}{E_T^4}, \tag{11}$$

$$\frac{d\hat{\sigma}_{\mathrm{excl}}}{dt}(gg \rightarrow q\bar{q}) = \frac{\pi \alpha_s^2}{6E_T^4} \frac{m_q^2}{M^2}\left(1 - \frac{4m_q^2}{M^2}\right), \tag{12}$$

where E_T is the transverse energy of the final state parton and m_q is the quark mass. The suppression of $gg \rightarrow q\bar{q}$ is due to the factor $(m_q^2/M^2)(1 - 4m_q^2/M^2)$, which vanishes as $m_q^2/M^2 \rightarrow 0$ ($J_z = 0$ selection rule [10]). Exclusive $gg \rightarrow q\bar{q}$ contributions are also strongly suppressed in NLO and NNLO QCD, and in certain higher orders [44].

The predicted exclusive $q\bar{q}$-dijet suppression offers the opportunity of searching for an exclusive signal in IDPE data by comparing the inclusive dijet R_{jj} shape with that of data containing identified $q\bar{q}$ dijets. The presence of an exclusive dijet signal in the IDPE event sample would be expected to appear as a suppression in the ratio of $q\bar{q}$ to inclusive events at high R_{jj}. This data driven method avoids the use of MC simulations and can be used to corroborate the MC-based extraction of the exclusive signal from the inclusive data sample. As many systematic effects cancel in measuring the ratio, a relatively small $q\bar{q}$ event sample can provide valuable information.

To ensure quark origin, we select jets from heavy flavor (HF) b- or c-quarks, identified from secondary vertices produced from the decay of intermediate B or D mesons using the SVX II detector. Both b- and c-quark jets are used, since the suppression mechanism holds for all quark flavors.

Below, in Sec. VIII A we describe the HF data sample and event selection requirements, in Sec. VIII B we evaluate the HF selection efficiencies and backgrounds, and in Sec. VIII C we present the HF-jet fraction results.

A. Data sample and event selection

The data used in this analysis were collected at a full rate (no prescaling) with a trigger satisfying the same requirements as the DPE trigger, $\mathrm{J5 \cdot RPS \cdot \overline{BSC1}_p}$, plus an additional one designed to enhance the HF-jet content. The latter required the presence of at least one track with transverse momentum $p_T > 2$ GeV/c displaced from the IP by a distance d of $0.1 < d < 1.0$ mm, where d is the distance of closest approach of the track to the IP [45]. The total integrated luminosity of this data sample is 200 ± 12 pb^{-1}.

Jets are reconstructed using a CDF Run I based iterative cone algorithm [46] with an η-ϕ cone of radius 0.4. The SECVTX tagging algorithm is used to search for a displaced secondary vertex due to a B or D meson decay within a jet cone. This algorithm seeks tracks with hits in the SVX II within the jet cone, and reconstructs the secondary vertex from those which are significantly displaced from the primary vertex. A jet is considered SECVTX tagged if it has a secondary vertex consisting of at least two (or three) such tracks with $p_T > 1(0.5)$ GeV/c. Events are further required to pass the IDPE selection criteria listed in Eq. (7). This selected "pretag" event sample contains 34 187 jets with at least two tracks in the SVX II. Applying the SECVTX tagging algorithm to the jets in the pretag sample yields 1118 tagged jets with $E_T^{\mathrm{jet}} > 10$ GeV and $|\eta^{\mathrm{jet}}| < 1.5$.

B. Heavy flavor selection efficiencies

A SECVTX tag in a jet without a HF quark is labeled as a "mistag." The mistag probability per jet, measured from inclusive jet data, is parametrized as a function of the number of tracks, E_T, η, and ϕ of the jet, and the sum over the E_T values of all jets with $E_T^{\mathrm{jet}} > 10$ GeV and $|\eta^{\mathrm{jet}}| < 2.4$ in the event. The mistag background in tagged

jets is estimated by weighting each jet in the pretag sample by the mistag probability and summing up the weights over all jets in the sample. The total number of mistag jets, N_{mistag}, is measured to be 104 ± 15. This number is consistent with a background estimate obtained from studies of the distribution of the invariant mass distribution M_{svtx} of charged particles associated with a displaced secondary vertex (Fig. 21). The mistag background for a given R_{jj} interval is evaluated by applying the mistag probability to the jets in that interval of the pretag sample.

The efficiency for tagging HF jets by the SECVTX algorithm depends on the composition of b- and c-jets of the data sample to which the algorithm is applied, and is therefore evaluated using a combination of a Monte Carlo simulation and HF-jet fractions obtained from the data. The tagging efficiency for a $b(c)$-jet, $\epsilon_b(\epsilon_c)$, is obtained using PYTHIA MC dijet events passed through a detector simulation, and is corrected for discrepancies observed between MC events and data. The fraction of $b(c)$-jets in the DPE data sample, $F_b(F_c)$, is obtained from the fit to the M_{svtx} distribution shape (Fig. 21). The tagging efficiency for a HF jet, $\epsilon_{tag}^{HF} = F_{HF}/[F_b/\epsilon_b + F_c/\epsilon_c]$, is found to be $7.9 \pm 1.4\%$ for $E_T^{jet} \sim 15$ GeV, where $F_{HF} = F_b + F_c$.

The data are corrected for efficiencies associated with the displaced track (DT) requirement in the trigger. These efficiencies are obtained from a data sample collected without requiring a displaced track. Selecting from this sample events that pass the DT requirement, we obtain the DT trigger efficiency for inclusive jets as the ratio $\epsilon_{all}^{DT} = N_{all}^{DT}/N_{all}$, where N_{all}^{DT} is the number of jets in the selected events and N_{all} is the total number of jets in the sample.
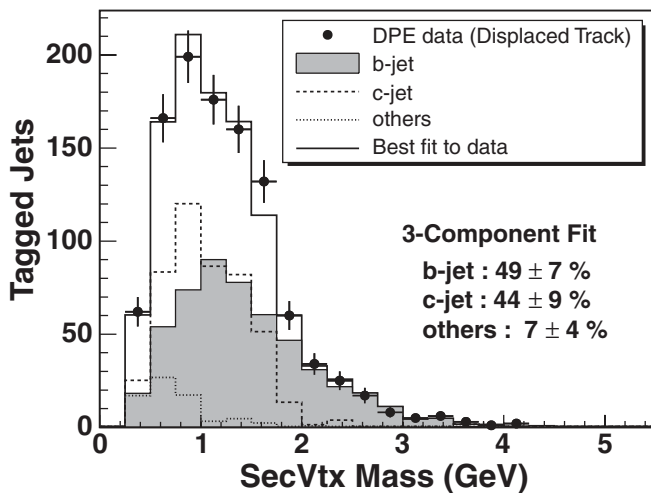

FIG. 21. Displaced secondary vertex mass distribution for jets tagged by the SECVTX algorithm in DPE data (points). The solid histogram shows the result of a three-component binned maximum likelihood fit to the data, using Monte Carlo templates of distribution shapes, consisting of b-jets (shaded histogram), c-jets (dashed histogram), and other jets (dotted histogram) obtained from PYTHIA dijet events.

Similarly, the efficiency for HF jets is obtained as $\epsilon_{HF}^{DT} = N_{HF}^{DT}/N_{HF} = [N_{tag}^{DT}(1 - F_{mistag}^{DT})]/[N_{tag}(1 - F_{mistag})]$, where N_{tag} (N_{tag}^{DT}) is the number of tagged jets and F_{mistag} (F_{mistag}^{DT}) the mistag background fraction in events without (with) the DT requirement. F_{mistag}^{DT} is evaluated from a 3-component MC template fit to the M_{svtx} data distribution, consisting of b-, c-, and other jets at experimentally measured proportions (Fig. 21), while F_{mistag} is measured from the corresponding M_{svtx} fit to the DPE data collected without the DT requirement.

C. Heavy flavor jet fraction results

Results for the fraction $F_{HF/incl}$ of HF jets to all inclusive jets of $E_T^{jet} > 10$ GeV and $|\eta^{jet}| < 1.5$ for the IDPE event sample are shown in Fig. 22(a) as a function of dijet mass fraction R_{jj}. The fraction is normalized to the mean value of the ratio of the HF to inclusive events over the four R_{jj} bins in the region of $R_{jj} < 0.4$, so that systematic uncertainties correlated among R_{jj} bins cancel out, as e.g. the uncertainties from corrections for data to MC tagging efficiency discrepancies or from the mistag background fraction estimate before and after the DT trigger requirement. Thus,

$$F_{HF/incl} = \langle F_{HF/incl} \rangle|_{R_{jj}<0.4} \cdot \frac{\sigma^{incl}}{\sigma^{incl} + \sigma^{excl}}, \quad (13)$$

where σ^{incl} is the inclusive DPE jet production cross section only, σ^{excl} is the exclusive cross section, and $\langle F_{HF/incl} \rangle|_{R_{jj}<0.4}$ is the mean value of $F_{HF/incl}$ in the range $R_{jj} < 0.4$ [47]. An exclusive dijet production rate contributing to the total rate but which is suppressed in HF dijet production would be expected to appear as a suppression in the fraction $F_{HF/incl}$ at high R_{jj} [43]. The suppression seen in Fig. 22(a) is examined here for consistency with this hypothesis.

The statistical uncertainties shown in Fig. 22 are dominated by the low statistics HF event sample. Measuring the fraction of HF to inclusive dijet events has the advantage of reducing systematic uncertainties common to both event samples. The fraction is corrected for mistag backgrounds, tagging efficiency for HF jets, and displaced track trigger efficiencies for inclusive and HF jets.

The systematic uncertainties on the ratio $F_{HF/incl}$, shown in Fig. 22 as shaded areas, are due to the uncertainties associated with the background and efficiency estimates. The mistag background uncertainty is evaluated from the uncertainties associated with the determination of the mistag probability and propagated to an uncertainty in the fraction. The HF-jet tagging efficiency, derived from combinations of PYTHIA MC generated events and data, has an uncertainty propagated from the statistical uncertainty of the MC generated event sample, uncertainties from the correction for discrepancies between the tagging efficien-
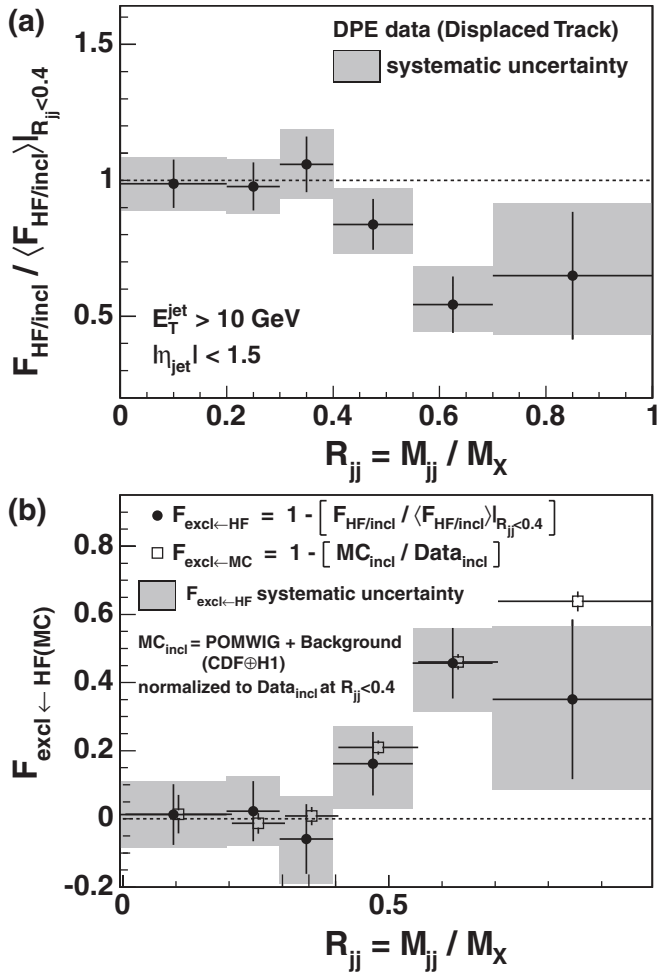
FIG. 22.   (a) Measured ratio $F_{HF/incl}$ of heavy flavor jets to all inclusive jets of $E_T^{jet} > 10$ GeV and $|\eta^{jet}| < 1.5$ as a function of dijet mass fraction R_{jj}, normalized to the weighted average value in the region of $R_{jj} < 0.4$, with systematic uncertainties represented by the shaded band; (b) values of $F_{excl\leftarrow HF} = 1 - F_1$ (filled circles) and $F_{excl\leftarrow MC} = 1 - F_2$ (open squares) as a function of R_{jj}, where $F_1 = F_{HF/incl}/<F_{HF/incl}>|_{R_{jj}<0.4}$, plotted in (a) vs R_{jj}, and F_2 is the ratio of POMWIG MC to inclusive dijet events obtained from the studies presented in Sec. VI—the error bars (shaded band) represent statistical ($F_{excl\leftarrow HF}$ systematic) uncertainties.

cies derived from MC and data, and uncertainties from the b- and c-jet fractions in the tagged jet data sample. The displaced track trigger efficiency has two sources of systematic uncertainty: the statistical uncertainty of the IDPE sample collected without the displaced track requirement, and the uncertainty on the mistag background fractions before and after applying the mistag requirement to the sample. In addition to the above uncertainties, we assign a systematic uncertainty associated with an increasing trend of c- to b-jet fraction found in PYTHIA generated events, which could contribute to a decreasing HF-jet fraction with R_{jj} due to the tagging efficiency ϵ_c being lower than ϵ_b.

To examine the consistency between the MC-based extracted exclusive dijet fraction and the data based suppression of the exclusive HF to inclusive dijet production rates we compare in Fig. 22(b) the R_{jj} residual distributions defined as $F_{excl\leftarrow MC} \equiv 1 - [MC_{incl}/Data_{incl}]$, for which the excess is defined as the inclusive DPE events observed above the inclusive R_{jj} distribution (composed of POMWIG MC events with ND and SD backgrounds) normalized to the DPE data at $R_{jj} < 0.4$ (open squares), and $F_{excl\leftarrow HF} \equiv 1 - [F_{HF/incl}/\langle F_{HF/incl}\rangle|_{R_{jj}<0.4}]$ (filled circles). The absolute values and R_{jj} dependence of the $F_{excl\leftarrow HF}$ points in the region of $0.4 < R_{jj} < 1.0$ are consistent with those of $F_{excl\leftarrow MC}$, supporting an interpretation of the observed $F_{HF/incl}$ distribution as a manifestation of the suppression of HF quark jets in exclusive production.

IX. EXCLUSIVE DIJETS AND DIFFRACTIVE HIGGS PRODUCTION

The search for Higgs bosons is one of the top priorities of the LHC experiments. While the main effort of both the ATLAS and CMS experimental plans is directed toward searches for inclusively produced Higgs bosons, an intense interest has developed toward exclusive Higgs boson production, $p + p \rightarrow p + H + p$ [48]. The exclusive Higgs production channel presents several advantages, including: (i) it can provide events in an environment of suppressed QCD backgrounds for the main Higgs decay mode of $H \rightarrow b_{jet} + \bar{b}_{jet}$, due to the $J_z = 0$ selection rule discussed in Sec. VIII, (ii) the Higgs mass can be measured accurately with the missing mass technique by detecting and measuring the momentum of the outgoing protons [49], (iii) the spin-parity of the Higgs boson can be determined from the azimuthal angular correlations between the two outgoing protons, and (iv) the method is universally sensitive to all exclusive Higgs production mechanisms.

Theoretical predictions for exclusive Higgs boson production cross sections range from ~ 200 fb [5] to $2-6$ fb [50] for a Higgs boson mass of ~ 120 GeV at $\sqrt{s} = 14$ TeV at the LHC. However, since exclusive Higgs boson and exclusive dijet production proceed through similar diagrams, as illustrated in Fig. 1(b) (with no Pomeron remnants) and Fig. 2, the models can be calibrated by comparing their predictions for exclusive dijet cross sections with measured values at the Tevatron. Furthermore, measured exclusive dijet cross sections at the Tevatron may also be used to evaluate backgrounds to the process $H \rightarrow b\bar{b}$ from exclusive gg dijet production with gluons misidentified as b-quarks in b-tagging, or from b-quarks produced by gluon splitting, $g \rightarrow b\bar{b}$.

A. M_{jj} distribution

The measured exclusive dijet cross section presented in Fig. 20 vs jet E_T^{min} is converted to a cross section vs dijet mass M_{jj} using the EXHUME Monte Carlo simulation with
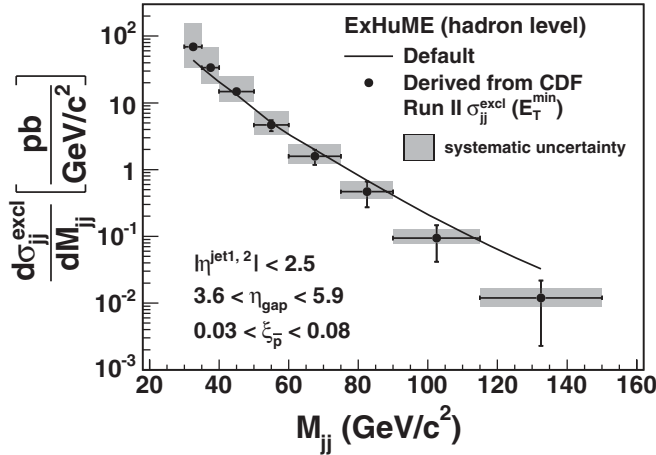
FIG. 23. EXHUME exclusive dijet differential cross section at the hadron level vs dijet mass M_{jj}. The filled points show cross sections derived from the measured $\sigma_{jj}^{\text{excl}}$ values shown in Fig. 20 (top) using the procedure described in the text. The vertical error bars on the points and the shaded band represent statistical and systematic uncertainties, respectively, obtained by propagating the corresponding uncertainties to the measured values of $\sigma_{jj}^{\text{excl}}$. The solid curve is the cross section predicted by EXHUME using the default settings.

M_{jj} reconstructed at the hadron level. From the measured values of $\sigma_{jj}^{\text{excl}}$ for the $E_T^{\text{jet1,2}}$ thresholds given in Table. III, we obtain the cross section for each of the following E_T^{jet2} intervals; 10–15 GeV, 15–20 GeV, 20–25 GeV, 25–35 GeV, and 35 GeV or higher. After applying a hadron-level E_T^{jet2} cut, the EXHUME M_{jj} distribution for each E_T^{jet2} interval is normalized to the cross section for that interval. Summing up over all the normalized M_{jj} distributions yields the EXHUME-based exclusive dijet differential cross section as a function of M_{jj}, $d\sigma_{jj}^{\text{excl}}/dM_{jj}$. The values obtained are corrected for a possible bias caused by the minimum threshold requirement of $E_T^{\text{jet2}} > 10$ GeV by comparing the M_{jj} distributions with and without the E_T^{jet2} cut. The derived $d\sigma_{jj}^{\text{excl}}/dM_{jj}$ distribution is shown for $M_{jj} > 30$ GeV/c^2 in Fig. 23 (solid circles). This distribution falls slightly faster than the default EXHUME prediction (solid curve), as one would expect from the fact that the measured $\sigma_{jj}^{\text{excl}}(E_T^{\min})$ falls somewhat more steeply with $E_T^{\min}$ than that of EXHUME (Fig. 20), but overall there is reasonable agreement. This result supports the EXHUME prediction, and thereby the perturbative QCD calculation of Ref. [6] on which EXHUME is based.

B. Higgs boson cross section

From the EXHUME resulting values of $d\sigma_{jj}^{\text{excl}}/dM_{jj}$, we obtain $\sigma_{jj}^{\text{excl}} \approx 360$ fb for the range $115 < M_{jj} < 145$ GeV/c^2, which corresponds to a $\pm 12\%$ mass window around $M_{jj} = 130$ GeV/c^2 for jets within the kinematic

region defined by the cuts denoted in Fig. 23. For SM Higgs boson production at the Tevatron, perturbative calculations [50] predict $\sigma_H^{\text{excl}} \sim 0.2$ fb with a factor of 2–3 uncertainty for a Higgs boson mass of $m_H = 120$ GeV/c^2, which leads to a ratio of exclusive Higgs signal to dijet background of $R_{H/jj} \sim 6 \times 10^{-4}$. This value is in agreement with the estimate of $R_{H/jj} = 6 \times 10^{-4}$ given in Ref. [50] for $m_H = 120$ GeV/c^2 using an experimental missing mass resolution of $\Delta M_{\text{missing}} = 3$ GeV/c^2 at the LHC, rendering support to the prediction of the SM Higgs exclusive production cross section of 3 fb (with a factor of 3 uncertainty) presented in Ref. [6]. Measurements of exclusive dijet production rates in the Higgs mass range at the LHC could further constrain σ_H^{excl} through $R_{H/jj}$.

Models of exclusive Higgs production may also be tested using measured cross sections for exclusive $\gamma\gamma$ production, $p + p \rightarrow p + \gamma\gamma + p$, a process similar to exclusive dijet production. In the model of Ref. [51], the $\gamma\gamma$ production is represented by the diagrams of Fig. 2 in which "jet" is replaced by "γ." A recent CDF measurement [52] yielded a cross section upper limit close to the predicted value, providing further support for this exclusive production model.

X. SUMMARY AND CONCLUSION

We have presented results from studies of dijet production in $\bar{p}p$ collisions at $\sqrt{s} = 1.96$ TeV using events with a leading antiproton detected in a Roman pot spectrometer and a forward rapidity gap on the outgoing proton side, collected by the CDF II detector during Fermilab Tevatron Run II. These events, presumed to be produced by double Pomeron exchange, were extracted from a data sample of integrated luminosity 310 pb^{-1}. In particular, we have demonstrated the presence of exclusively produced dijets, $\bar{p} + p \rightarrow \bar{p} + \text{dijet} + p$, by means of detailed studies of distributions of the dijet mass fraction R_{jj}, defined as the dijet mass divided by the DPE system mass. In comparisons of data R_{jj} distributions with inclusive POMWIG [23] Monte Carlo simulations, we observe an excess of events in the data over the Monte Carlo predictions at high R_{jj}, which is consistent in terms of kinematic distribution shapes with the presence of an exclusive dijet signal as modeled by the EXHUME [34] and exclusive DPE in DPEMC [35] Monte Carlo simulations. To facilitate comparison with theoretical predictions, the exclusive dijet cross section, $\sigma_{jj}^{\text{excl}}$, and the ratio of exclusive dijet to inclusive DPE dijet cross sections have been measured as a function of minimum E_T threshold of the two leading jets in an event. The measured values of $\sigma_{jj}^{\text{excl}}$ favor the EXHUME over the DPEMC predictions, and are found to be consistent with predictions from perturbative calculations presented in Ref. [6].

The Monte Carlo based extraction of the exclusive dijet signal is checked experimentally using a largely indepen-

dent sample of heavy flavor b-tagged jet events extracted from 200 pb^{-1} of DPE data collected with a special trigger requiring a track displaced from the interaction point. As exclusive dijet production from $gg \to q\bar{q}$ is predicted to be suppressed by the $J_Z = 0$ selection rule relative to production through $gg \to gg$, the ratio of identified heavy flavor quark jets to inclusive jets is expected to decrease at high R_{jj}. For jets of $E_T^{\text{jet}} > 10$ GeV, we observe a suppression of the ratio of heavy flavor jets to inclusive jets in the region of $R_{jj} > 0.4$, which is consistent in shape and magnitude with the expectation from the exclusive signal extracted by the MC-based method based on Ref. [6].

The present results, representing the first observation of exclusive dijet production in high energy $\bar{p}p$ collisions, provide a benchmark template against which to calibrate theoretical calculations of exclusive Higgs boson production. The prospects for an observation of exclusive Higgs boson production at the LHC have been briefly discussed in light of our measured exclusive dijet cross sections.

[1] G. Ingelman and P. Schlein, Phys. Lett. **152B**, 256 (1985).

[2] T. Affolder *et al.* (CDF Collaboration), Phys. Rev. Lett. **85**, 4215 (2000).

[3] Rapidity, $y = \frac{1}{2} \ln \frac{E + p_L}{E - p_L}$, and pseudorapidity, $\eta = -\ln\tan\frac{\theta}{2}$, are used interchangeably for particles detected in the calorimeters, since in the kinematic range of interest in this analysis they are approximately equal.

[4] While the exclusive DPE process is part of the inclusive, it has become traditional to refer to the processes with and without Pomeron remnants as ''inclusive'' and ''exclusive,'' respectively. In this paper we will follow this tradition.

[5] A. Bialas and P. V. Landshoff, Phys. Lett. B **256**, 540 (1991).

[6] V. A. Khoze, A. D. Martin, and M. G. Ryskin, Eur. Phys. J. C **14**, 525 (2000).

[7] M. Boonekamp, R. Peschanski, and C. Royon, Phys. Lett. B **598**, 243 (2004), and references therein.

[8] We use a coordinate system with origin at the center of the CDF detector, z coordinate along the proton beam direction, and y coordinate pointing up; the x coordinate points away from the center of the accelerator ring.

[9] A. Berera, Phys. Rev. D **62**, 014015 (2000).

[10] V. A. Khoze, A. D. Martin, and M. G. Ryskin, Eur. Phys. J. C **19**, 477 (2001); **20**, 599 (2001).

[11] D. Acosta *et al.* (CDF Collaboration), Phys. Rev. D **71**, 032001 (2005).

[12] A. Sill *et al.*, Nucl. Instrum. Methods Phys. Res., Sect. A **447**, 1 (2000).

[13] A. Affolder *et al.*, Nucl. Instrum. Methods Phys. Res., Sect. A **526**, 249 (2004).

[14] L. Balka *et al.*, Nucl. Instrum. Methods Phys. Res., Sect. A **267**, 272 (1988).

[15] S. Bertolucci *et al.*, Nucl. Instrum. Methods Phys. Res., Sect. A **267**, 301 (1988).

[16] M. Albrow *et al.*, Nucl. Instrum. Methods Phys. Res., Sect. A **480**, 524 (2002).

[17] K. Goulianos, *DIFFRACTION 2006 - International Workshop on Diffraction in High-Energy Physics, Adamantas, Milos Island, Greece, 2006* [Proc. Sci., DIFF2006 (2006) 016].

[18] M. Gallinaro *et al.*, Nucl. Instrum. Methods Phys. Res., Sect. A **496**, 333 (2003).

[19] D. Acosta *et al.*, Nucl. Instrum. Methods Phys. Res., Sect. A **494**, 57 (2002).

[20] G. C. Blazey *et al.*, arXiv:hep-ex/0005012.

[21] T. Sjöstrand *et al.*, Comput. Phys. Commun. **135**, 238 (2001).

[22] E. Gerchtein and M. Paulini, in *CDF Detector Simulation Framework and Performance*, eConf C0303241, TUMT005 (2003).

[23] B. E. Cox and J. R. Forshaw, Comput. Phys. Commun. **144**, 104 (2002).

[24] T. Affolder *et al.* (CDF Collaboration), Phys. Rev. Lett. **84**, 5043 (2000).

[25] J. Pumplin, D. R. Stump, J. Huston, H. L. Lai, P. Nadolsky, W. K. Tung, J. High Energy Phys. 07 (2002) 012.

[26] K. Goulianos, Proc. Sci., DIFF2006 (2006) 016.

[27] F. Abe *et al.* (CDF Collaboration), Phys. Rev. Lett. **78**, 2698 (1997); **79**, 2636 (1997); T. Affolder *et al.* (CDF Collaboration), Phys. Rev. Lett. **84**, 232 (2000).

[28] C. Adloff *et al.* (H1 Collaboration), Z. Phys. C **76**, 613

(1997).

[29] The maximum value of Q^2 in the H1 x2 fit3 Pomeron PDF is 75 GeV^2 and is used as a default setting in the POMWIG generator.

[30] S. Chekanov *et al.* (ZEUS Collaboration), Eur. Phys. J. C **38**, 43 (2004).

[31] S. Chekanov *et al.* (ZEUS Collaboration), Nucl. Phys. **B713**, 3 (2005).

[32] M. Groys, A. Levy, and A. Proskuryakov, arXiv:hep-ex/0601013.

[33] A. Aktas *et al.* (H1 Collaboration), Eur. Phys. J. C **48**, 715 (2006); arXiv:hep-ex/0606004.

[34] J. Monk and A. Pilkington, Comput. Phys. Commun. **175**, 232 (2006); arXiv:hep-ph/0502077.

[35] M. Boonekamp and T. Kucs, Comput. Phys. Commun. **167**, 217 (2005); arXiv:hep-ph/0312273.

[36] A. D. Martin *et al.*, Eur. Phys. J. C **28**, 455 (2003).

[37] G. Corcella *et al.*, J. High Energy Phys. 01 (2001) 010; arXiv:hep-ph/0210213.

[38] S. Klimenko, J. Konigsberg, and T. Liss, Report No. FERMILAB-FN-0741, 2003.

[39] A. Affolder *et al.* (CDF Collaboration), Phys. Rev. D **65**, 092002 (2002).

[40] V. A. Khoze, A. B. Kaidalov, A. D. Martin, M. G. Ryskin, W. J. Stirling, in *Gribov Memorial Vol., Proceedings of the Memorial Workshop Devoted to the 75th Birthday of V. N. Gribov, Budapest, Hungary, 2005*, edited by Yu. L. Dokshitzer, P. Lévai, and J. Nyíri (World Scientific, Singapore, 2006) p. 129.

[41] V. A. Khoze and M. G. Ryskin (private communication).

[42] V. A. Khoze, A. D. Martin, and M. G. Ryskin, arXiv:0705.2314.

[43] V. A. Khoze, A. D. Martin, and M. G. Ryskin, Eur. Phys. J. C **23**, 311 (2002).

[44] V. A. Khoze, M. G. Ryskin, and W. J. Stirling, arXiv:hep-ph/0607134v1.

[45] W. Ashmanskas *et al.*, Nucl. Instrum. Methods Phys. Res., Sect. A **518**, 532 (2004).

[46] F. Abe *et al.* (CDF Collaboration), Phys. Rev. D **45**, 1448 (1992).

[47] We assume that in the region of $R_{jj} < 0.4$ there is no HF contribution from exclusive jet production (see Fig. 14), so that $\sigma_{HF}/\sigma^{\text{incl}} = \sigma_{HF}^{\text{incl}}/\sigma^{\text{incl}} = \langle F_{HF/\text{incl}} \rangle|_{R_{jj}<0.4}$, where $\sigma_{HF}^{\text{incl}}$ is the HF-jet cross section obtained from inclusive DPE events.

[48] *FP420, An R&D Proposal to Investigate the Feasibility of Installing Proton Tagging Detectors in the 420m Region of the LHC*, Report No. CERN-LHCC-2005-025, http://www.fp420.com.

[49] M. G. Albrow and A. Rostovtsev, arXiv:hep-ph/0009336.

[50] A. B. Kaidalov, V. A. Khoze, A. D. Martin, and M. G. Ryskin, Eur. Phys. J. C **31**, 387 (2003); **33**, 261 (2004).

[51] V. A. Khoze, A. D. Martin, M. G. Ryskin, and W. J. Stirling, Eur. Phys. J. C **38**, 475 (2005).

[52] T. Aaltonen *et al.* (CDF Collaboration), Phys. Rev. Lett. **99**, 242002 (2007).